Master's Thesis (Academic Year 2022)

Upgrade of Two Dimensional Track Trigger on Central Drift Chamber aimed for Belle II Targeted Luminosity

（Belle IIの高輝度化に向けた２次元飛跡トリガー装置のアップグレード）

the University of Tokyo
Department of Physics, Graduate School of Science

Ping Ni

August 9th, 2022

ABSTRACT

The Belle II experiment hosted by KEK has started taking physics data since 2019, committed to finding new physics beyond the Standard Model. The SuperKEKB has been upgraded to collide e^- and e^+ beams with a designed luminosity of $6 \times 10^{35}\,\mathrm{cm}^{-2}\mathrm{s}^{-1}$ which is 30 times higher than the predecessor, the Belle experiment.

Accompanied by the higher luminosity is the higher beam-originated background, making it challenging to operate the Level-1 trigger system while keeping high efficiency for physics events and trigger rate smaller than the limit of 30 kHz. We evaluate the performance of the 2D track trigger at the designed luminosity with Monte Carlo simulation and clarify that the trigger rate is expected to exceed the limit of 30 kHz due to fake tracks. An upgraded 2-dimensional tracking algorithm named "Full-hit algorithm" has been developed in order to resolve this issue. The algorithm is designed as a simulation software and succeeded in reducing the trigger rate from the fake tracks below 1 kHz. The algorithm is optimized as a digital circuit on the Field Programmable Gate Array and successfully implemented in a new generation of the Belle II universal trigger board. The Full-hit is under commissioning and is planned to be used for physics operation in 2023 after the long shutdown of the Belle II.

Contents

Chapter 1

Introduction

The Belle II experiment [1] is a particle physics experiment conducted at the SuperKEKB accelerator located in Tsukuba Japan. The predecessor, the Belle experiment [2] firstly observed large signals of CP violation in the B meson sector in 2001, which provided a solid experimental foundation for Kobayashi and Maskawa's theory [3]. The Belle II is designed to more precisely measure weak interaction parameters and find new physics beyond the Standard Model (SM). The KEKB at which the Belle was conducted, was an energy-asymmetric e^-e^+ collider and had been holding the world-record luminosity for long years. The SuperKEKB is upgraded from the KEKB to achieve even higher luminosity to the 30-fold than the KEKB by the Nano-beam Scheme as will be described in Section 2.2.2. The center-of-mass energy of the SuperKEKB beams is 10.58 GeV, at the $\Upsilon(4S)$ resonance, which is the same as the KEKB. However, the asymmetry of the beam energies is changed and hence the boost of the center-of-mass frame is smaller than the KEKB. Because more than 96% of $\Upsilon(4S)$s decay into $B\bar{B}$, the Belle/Belle II experiment is known as B-factory. With more than 30 times the higher luminosity, the Belle II is able to measure critical parameters in heavy-flavor physics as will be described in Section 2.1 and explore dark sector physics with better sensitivity. The Belle II has started its full operation and has been accumulating physics data from 2019. In June 2022, the SuperKEKB set a world-record luminosity of $4.7 \times 10^{34}\,\mathrm{cm}^{-2}\mathrm{s}^{-1}$.

The Belle II detector is a comprehensive detector composed of many subsystems to directly measure the vertex, charge, momentum, energy, and velocity of all long-lifetime charged particles, and neutral particles such as K_S, K_L and photons. Because of the asymmetric beam energy, the coverage of the Belle II detector in polar angle is designed to be $17^\circ - 150^\circ$ with a tendency to the direction of the electron beam which is higher in energy.

The trigger system is committed to selecting the events to be recorded. In the Belle II experiment, it is a two-stage system separated into the Level-1 trigger and the High-Level Trigger (HLT). The Level-1 trigger is based on electric circuits with the field-programmable gate array (FPGA), while the HLT is based on software. Events are preliminarily built in the Level-1 trigger to reduce the load of the Data-Acquisition system (DAQ) by limiting the trigger rate within 30 kHz at the design maximum. The data of the events satisfying the preset conditions in the Level-1 trigger can be transferred from the buffer to the DAQ. The HLT further filters out background events to relieve the burden on data storage.

The Central Drift Chamber (CDC) Trigger is one of the main sub-trigger systems in the Level-1 trigger and is also called "track trigger". To satisfy the specified latency of 4.2 μs from collision, the track trigger has to use a fast, stable, and time-constant tracking algorithm instead of directly imitating the tracking

algorithm used in the HLT. On the present track trigger, CDC hits are combined into units named "track segment" as will be described in Section 3.3.2 to reduce the size of processed data while achieving high reconstruction efficiency. The track trigger firstly reconstructs 2-dimensional tracks (2D track) by the 2D track trigger, based on which 3-dimensional tracks (3D track) are reconstructed by the 3D track trigger. The technique of "Hough transformation" is used in the 2D track trigger as the core logic.

As the beams will be 20 times more focused by the Nano-beam Scheme, the beam-originated background is expected to be several tens of times higher at the targeted luminosity. The beam-originated background hits in the CDC result in wrongly reconstructed tracks, which are called fake tracks. The increasing number of fake tracks can make the trigger rate purely caused by fake tracks about 5 times higher than the limit of 30 kHz. The algorithm has been developed in order to resolve this problem. An upgraded algorithm of the 2D track trigger has been designed as a simulation software targeted to suppress the trigger rate from fake tracks below 1 kHz, which algorithm is named "Full-hit algorithm". After that, the algorithm is optimized as a digital circuit on an FPGA and implemented in a new generation of the Belle II universal trigger board. The Full-hit is planned to be used for physics operation in 2023 after the long shutdown of the Belle II.

The contents of the following Chapters are as follows. In Chapter 2, we discuss the basic structure of the experiment including the accelerator and the detector sub-systems. In Chapter 3, we discuss the Level-1 trigger system, with a detailed explanation of the track trigger in general and the 2D track trigger. In Chapter 4, we discuss the performance evaluation of the 2D track trigger at each beam background level. In Chapter 5, we discuss the design of the Full-hit and the effect of suppressing the fake tracks. In Chapter 6, we discuss the implementation of the Full-hit as a digital circuit on an FPGA and introduce some preliminary commissioning works. In Chapter 7, the achievements in the studies are summarized. w

Chapter 2

The Belle II Experiment

In this chapter, the important features of the SuperKEKB collider and the sub-detectors in the Belle II experiment are introduced.

One of the physical motivations of the Belle II experiment is discussed in Section 2.1. The SuperKEKB accelerator at which the Belle II experiment is introduced in Section 2.2. The beam originated background of several patterns is explained in Section 2.3. The Belle II detector and its detector sub-systems are introduced in Section 2.4. As this thesis is focused on the track trigger, the introduction of the Central Drift Chamber (CDC) is expanded independently in Section 2.5.

2.1 Physical Motivation

The Belle II experiments challenge a wide range of physics, one of which is the more precise measurements of the CKM matrix [3]. Here gives a basic introduction to the CKM matrix.

The CKM matrix is a 3×3 unitary matrix denoted as

$$\mathrm{V} = \begin{pmatrix} V_{ud} & V_{us} & V_{ub} \\ V_{cd} & V_{cs} & V_{cb} \\ V_{td} & V_{ts} & V_{tb} \end{pmatrix}, \mathrm{V}\mathrm{V}^{\dagger} = 1, \tag{2.1}$$

in which $|V_{ij}|^2$ is proportional to the probability of transition from flavor j to flavor i by weak interaction. The CKM matrix can convert the mass eigenstates of down-type quarks to the weak eigenstates of down-type quarks as shown in Eq. 2.2.

$$\begin{pmatrix} d' \\ s' \\ b' \end{pmatrix} = \mathrm{V} \begin{pmatrix} d \\ s \\ b \end{pmatrix}, \tag{2.2}$$

where (d', s', b') is the weak eigenstates and (d, s, b) is the mass eigenstate.

The CKM matrix can be parameterized by 4 free parameters: θ_{ij} and CP-violating phase δ where ij can be 12, 13, or 23 as shown in Eq. 2.3.

$$\mathrm{V} = \begin{pmatrix} c_{12}c_{13} & s_{12}c_{13} & s_{13}e^{-i\delta} \\ -s_{12}c_{13} - c_{12}s_{23}s_{13}e^{i\delta} & c_{12}c_{23} - s_{12}s_{23}s_{13}e^{i\delta} & s_{23}c_{13} \\ s_{12}s_{13} - c_{12}c_{23}s_{13}e^{i\delta} & -c_{12}s_{23} - s_{12}c_{23}s_{13}e^{i\delta} & c_{23}c_{13} \end{pmatrix}, \tag{2.3}$$

where c_{ij} denotes $\cos\theta_{ij}$ and s_{ij} denotes $\sin\theta_{ij}$. From the unitarity of the CKM, $\mathrm{V}^{\dagger}\mathrm{V} = 1$ should hold true. One of the results that is the most relevant to B physics is from the 1st row and 3rd coulomb of $\mathrm{V}^{\dagger}\mathrm{V}$ which is

$$V_{ud}^{*}V_{ub} + V_{cd}^{*}V_{cb} + V_{td}^{*}V_{tb} = 0. \tag{2.4}$$

By dividing the equation by $V_{cd}^* V_{cb}$, we can derive

$$\frac{V_{ud}^* V_{ub}}{V_{cd}^* V_{cb}} + 1 + \frac{V_{td}^* V_{tb}}{V_{cd}^* V_{cb}} = 0. \tag{2.5}$$

It is obvious that 1, $\frac{V_{ud}^* V_{ub}}{V_{cd}^* V_{cb}}$ and $\frac{V_{td}^* V_{tb}}{V_{cd}^* V_{cb}}$ can constitute a triangle in a complex plane. The three angles in the triangle are respectively defined as

$$\phi_1 = \arg\left(-\frac{V_{cd}^* V_{cb}}{V_{td}^* V_{tb}}\right), \phi_2 = \arg\left(-\frac{V_{td}^* V_{tb}}{V_{ud}^* V_{ub}}\right), \phi_3 = \arg\left(-\frac{V_{ud}^* V_{ub}}{V_{cd}^* V_{cb}}\right). \tag{2.6}$$

The ϕ_1 and the ϕ_2 are determined by time-dependent CP asymmetries, which is a main field to which the Belle II collaboration is committed. Table 2.1 shows that the expected experimental uncertainties for the measurement of phi_1 and phi_2 are respectively expected to be about 1/3 and about 1/7 of that in the Belle, with the expected integrated luminosity of $50\,\mathrm{ab}^{-1}$ [4].

Table 2.1: Summary of the current and expected sensitivities on the CKM angle phi_1 and phi_2 by the Belle and the Belle II with an expected integrated luminosity of $50\,\mathrm{ab}^{-1}$ [4].

	Belle	Belle II
phi_1:		
Experimental	0.7°	0.2°
Theoretical: QCDF and pQCD	0.1°	0.1°
Theoretical: SU(3)	1.7°	0.8°
phi_2:		
Experimental	4.2°	0.6°
Theoretical	1.2°	$< 1.0°$

2.2 SuperKEKB

In this section, We discuss the basic configuration of the SuperKEKB, the nano-beam scheme that helps the SuperKEKB achieve 30 times higher luminosity, and the beam background.

2.2.1 Basic Configuration of the SuperKEKB

As shown in Fig. 2.1, the SuperKEKB is composed of a 1-km-long linear accelerator (LINAC) for electrons and positions, a damping ring that reduces the emittance of positrons, and a 3-km-long main storage ring for electrons and positrons. The electrons and the positrons are accelerated to near the required energy by the LINAC, and preserve the energy at the main storage ring. The intersection of the two beams is called interaction point (IP). Like other high-energy accelerators, Each accelerator in the SuperKEKB uses RF tubes. Therefore, beams are generated and stored as beam bunches. The present targeted luminosity of the SuperKEKB is $6 \times 10^{35}\,\mathrm{cm}^{-2}\mathrm{s}^{-1}$. The center-of-mass energy is mainly set at 10.58 GeV, which is the resonance energy of $\Upsilon(4S)$. The energy of the electrons is 7 GeV and that of the positrons is 4 GeV. Therefore, the storage ring of electrons is called HER (High Energy Ring), while that of positrons is called as LER (Low Energy Ring). To deduct the effect of background events unrelated to $\Upsilon(4S)$, 10.52 GeV is also a main energy section to obtain the continuum spectrum.

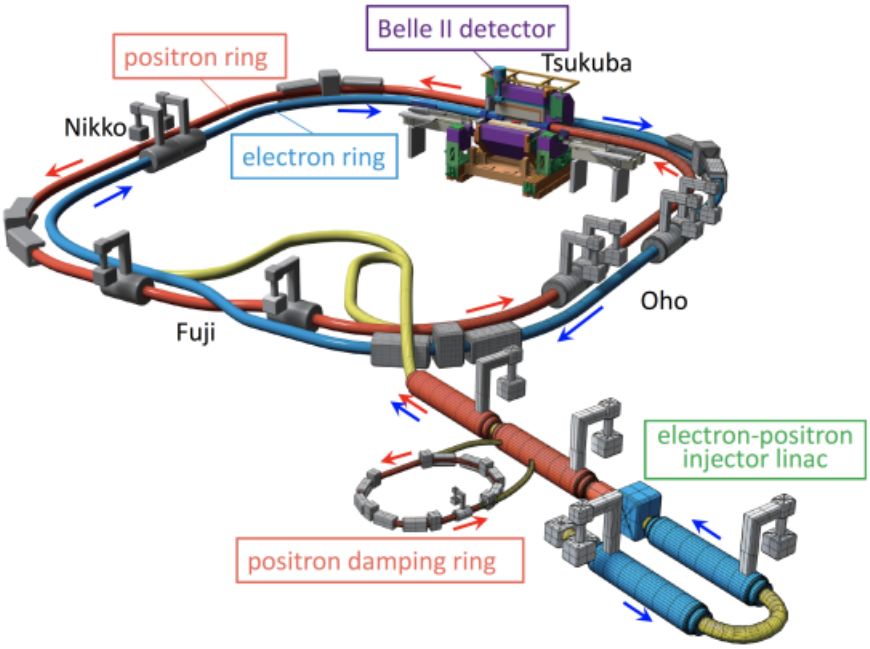

Figure 2.1: The SuperKEKB is composed of a linear accelerator (LINAC), a damping ring, and a main storage [5]

2.2.2 Nano-beam Scheme

Luminosity is determined by the following equation [6]:

$$L = \frac{\gamma_\pm}{2er_e}(1 + \frac{\sigma_y^*}{\sigma_x^*})\frac{I_\pm \xi_{y\pm}}{\beta_y^*}(\frac{R_L}{R_{\xi_{y\pm}}}) \tag{2.7}$$

where $+$ and $-$ denote positrons and electrons respectively, $\gamma_\pm$ are the Lorentz factors, r_e is the classical electron radius, $\sigma_{x,y}^*$ are the horizontal and vertical beam sizes of the perpendicular face at the IP, $I_\pm$ is the beam currents, $\xi_{y\pm}$ is the beam-beam tune-shift parameters, β_y^* is the vertical beta function at IP, and R_x is the correction factor related to parameter "x". The designed values of the parameters are shown in Table 2.2.

Table 2.2: Fundamental parameters of the SuperKEKB [6]

	LER	HER
Energy (GeV)	4.000	7.007
σ_x^* (μs)	10.1	10.7
σ_y^* (ns)	48	62
ξ_y	0.0881	0.0807
β_y^* (mm)	0.27	0.30
I (A)	3.6	2.6
Luminosity ($\mathrm{cm^{-2}s^{-1}}$)	80×10^{34}	

From Eq. 2.7, we can learn that the beam currents, tune-shift parameters, and beta functions are three kinds of changeable parameters to increase luminosity. The SuperKEKB was designed to achieve one-twentieth of the vertical beta function and double-fold beam current than the KEKB, therefore the targeted luminosity is set at around $6 \times 10^{35}\,\mathrm{cm^{-2}s^{-1}}$. To achieve such a small beta function,

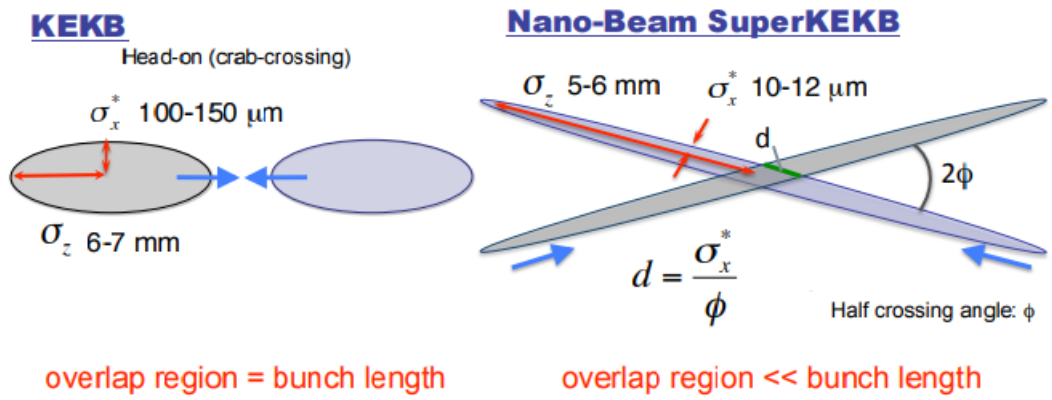

Figure 2.2: Nano-Beam Scheme [7]. The overlapping region of the beam bunches is greatly condensed in the SuperKEKB, which reduces the effective bunch length in order to aviod beam-beam effect.

the vertical beam size at the IP σ_y^* is focused to $50 - 60\,\mathrm{nm}$, which is the source of the name "nano-beam scheme". Actually, luminosity can hardly be further increased by squeezing β_y^* when β_y^* is as small as the bunch length because of the beam-beam effect. To avoid the beam-beam effect, the SuperKEKB collides the electrons and the positrons with a half crossing angle phi of 41.5 mrad as shown in Fig. 2.2. The effective bunch length d becomes σ_x^*/phi, which is smaller than 0.3 mm. As a result, squeezing β_y^* to 0.3 mm is expected to be a practical way to increase the luminosity.

2.3 Beam Background

Beam background can be categorized into two types: luminosity background and single-beam background. The luminosity background is the ordinary and uninteresting physics events such as Bhabha scattering. The amount of the luminosity background is proportional to the luminosity. The single-beam background is the background from the mechanism of the beam itself, including Touschek radiation, beam-gas scattering which includes coulomb scattering and Bremsstrahlung radiation, synchrotron radiation, etc. For the effect on the Central Drift Chamber (CDC), Touschek scattering and beam-gas scattering are two main components of the single-beam background and are paid attention to.

2.3.1 Touschek Scattering

Within a beam bunch, beam particles can interact with each other and some of them may deviate from the aperture of the ring. Such particles may well hit the vacuum chamber or magnet walls and generate an electromagnetic shower that affects detectors, which is called Touschek scattering. The intensity of Touschek scattering is proportional to

$$\frac{I^2}{\sigma_y n_b E^3}, \tag{2.8}$$

where I is the current, σ_y is the vertical bunch size, n_b is the number of beam bunches, and E is the beam energy [8]. The effect from horizontal bunch size is neglected because σ_y is much smaller than σ_x, resulting in much higher Touschek scattering. Because of the dependency on beam energy, Touschek scattering is

expected to be much stronger for LER than HER. In the Belle II, the extremely small σ_y of $50 - 60\,\text{nm}$ and doubled current make Touschek scattering a highly focused kind of beam background.

2.3.2 Beam-gas Scattering

The beam particles do not only interact with other beam particles in the same bunch, but also with the residual gas molecules in the beam pipe. Some of the beam particles may deviate from the aperture by the interaction with the residual gas molecules and cause an electromagnetic shower affecting detectors, which is called beam-gas scattering. There are mainly two kinds of beam-gas scattering: Coulomb scattering and Bremsstrahlung radiation. The Coulomb scattering is the dominant one in the beam-gas scattering. The effect of beam-gas scattering for a certain sub-detector is proportional to the current I and the pressure P. The pressure in beam pipes has a linear correlation with the current $P = P_0 + kI$, where P_0 is basic pressure without beam and k is a coefficient. Therefore, the beam-gas scattering is proportional to

$$I(P_0 + kI), \tag{2.9}$$

which includes a quadratic term with the current like Touschek scattering.

2.3.3 Geometrical Distribution of Beam Background

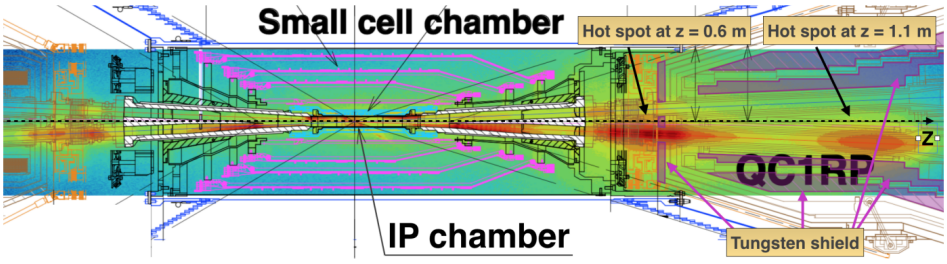

Figure 2.3: Top view of the vertices reconstruction studies in 2019. Hot spots in the forward region correspond to locations where particles producing background are lost [9].

Figure 2.3 shows the top view of the vertices of background events, which is based on the operation in 2019 [9]. Two main sources of the beam background are clearly visible at $z = 0.6\,\text{m}$ and $z = 1.1\,\text{m}$. One of the final focus superconducting magnets (QCS) is located at $z = 1.1\,\text{m}$ and the beam pipe is very narrow, which makes it the main source of the single beam background. By the beam background particles from $z = 1.1\,\text{m}$. The secondary particles concentrate around $z = 0.6\,\text{m}$. As the tungsten shield at $z = 0.6\,\text{m}$ is thinner than that $z = 1.1\,\text{m}$, the hot spot at $z = 0.6\,\text{m}$ is more visible.

2.4 Belle II Detector

As shown in Fig. 2.4, the Belle II detector is composed of seven sub-detectors from inner to outer: Pixel Vertex Detector (PXD), Silicon Vertex Detector (SVD), Central Drift Chamber (CDC), Time of Propagation Detector (TOP), Aerogel Ring-Imaging Cherenkov Detector (ARICH), Electromagnetic Calorimeter

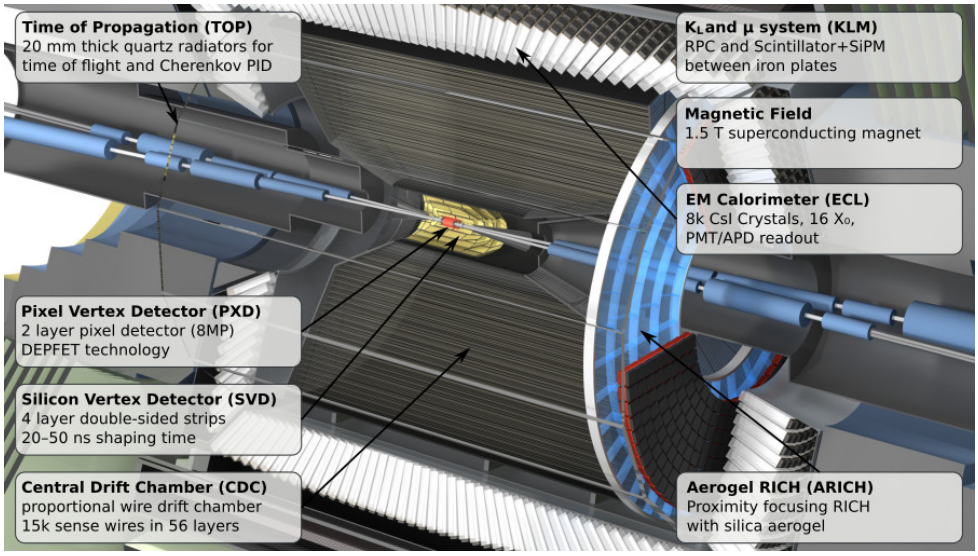

Figure 2.4: The Belle II Detector and the sub-detectors [10]

(ECL), Klong and Muon System (KLM) [1]. A 1.5 T Superconducting Magnet is set between the ECL and the KLM. The detailed design of the BelleII detector is shown in Fig. 2.5. As the CDC is the sub-detector most relevant to this study, the introduction of it is detailed in the next section.

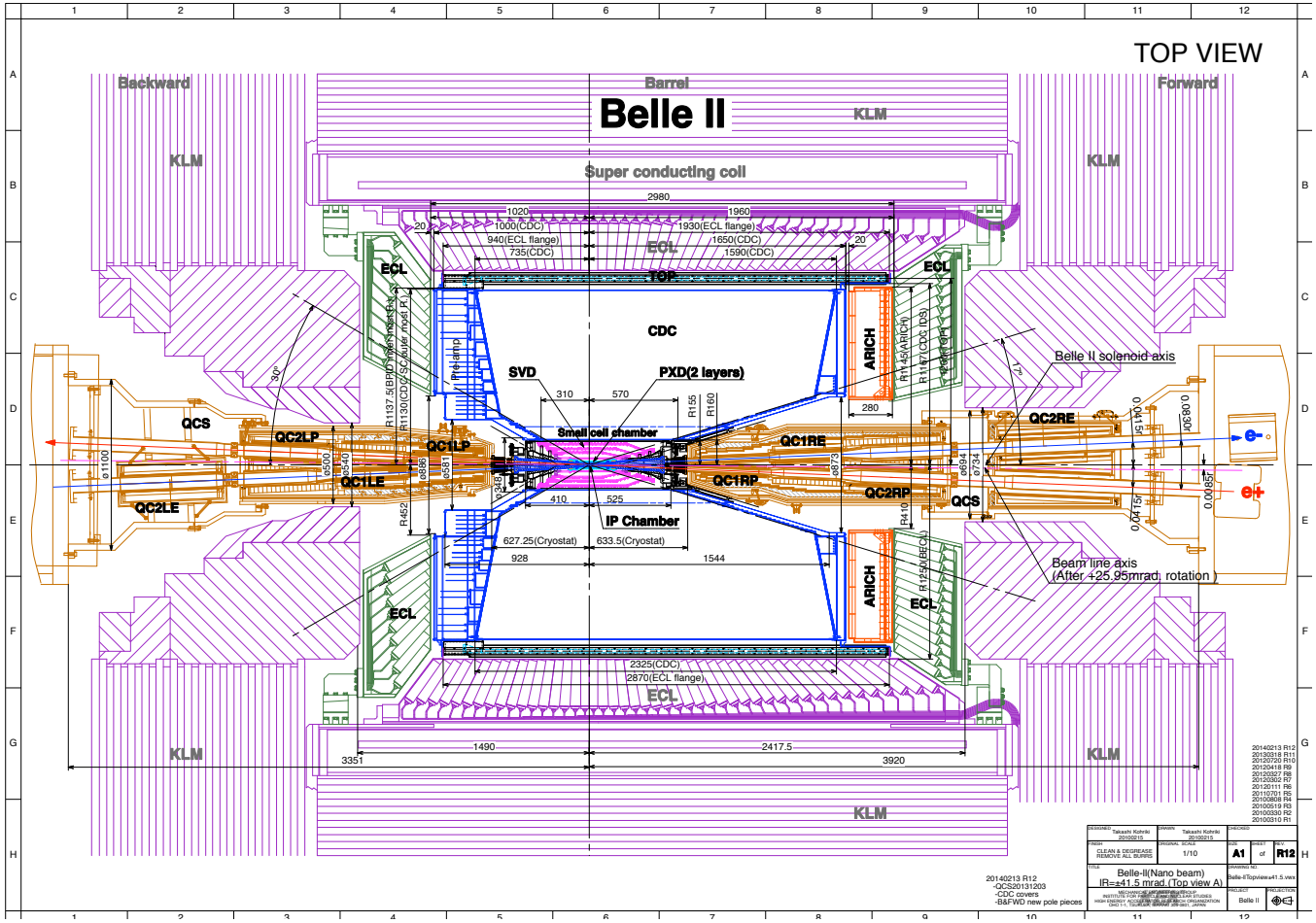

Figure 2.5: Designed structure of the Belle II detector from the top view [1]

2.4.1 Vertex Detector

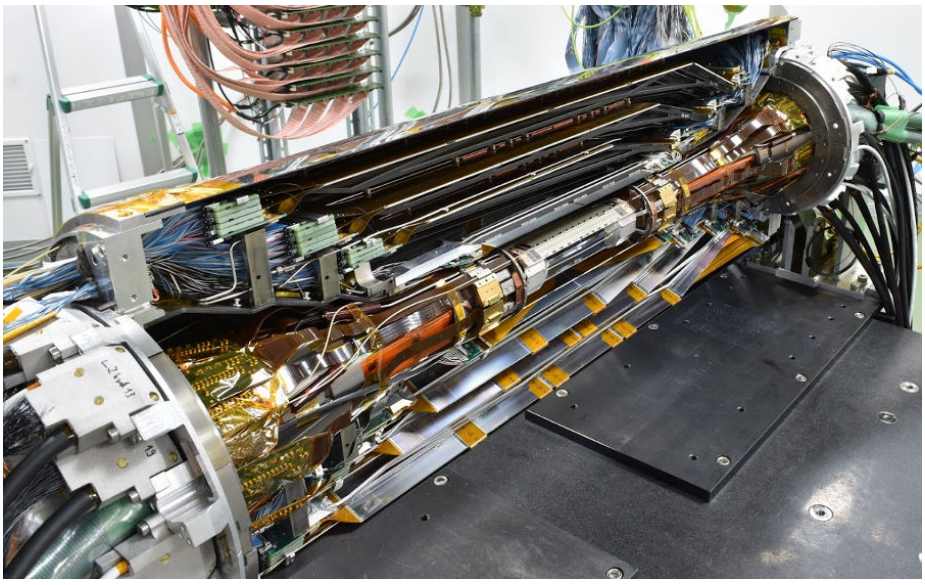

Figure 2.6: A real photo of the Vertex Detector. The inner 2 layers are PXD and the outer layers are SVD [11].

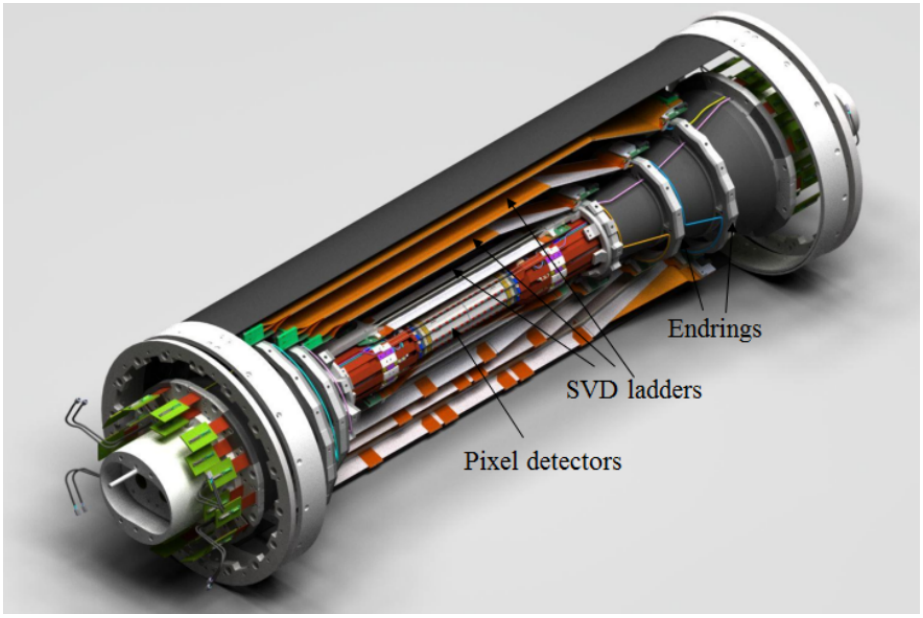

Figure 2.7: The configuration of the Vertex Detector [12]

Vertex is the intersection of tracks, which is usually the place where the tracks come from. The Pixel Vertex Detector (PXD) is the inner vertex detector with two layers and the Silicon Vertex Detector (SVD) is the outer Vertex Detector of the vertex detector with four layers. They are installed in one unit as shown in Fig. 2.6 and Fig. 2.7.

The PXD is constructed from Depleted P-channel Field Effect Transistor (DEPFET) silicon sensors segmented into individual eight million pixels. The size of every pixel is very small down to $50 \times 55\,\mu\text{m}^2$. The two layers are respectively located at layers at 14 mm and 22 mm radius from IP.

The SVD is composed of double-sided silicon micro-strip sensors. The width of the strips is as narrow as 50 μm. Unlike the PXD able to measures the 2D position directly, the SVD separately measures the horizontal and vertical position.

2.4.2 Particle Identification (PID) Detector

The Time of Propagation Detector (TOP) and the Aerogel Ring-Imaging Cherenkov Detector (ARICH) are two Particle Identification (PID) detectors in the Belle II. They can measure the velocity of particles. As an important reference for PID, the mass of a particle can be calculated by the formula $m_0 = \frac{p}{\gamma v}$, in which m_0 is the measured mass of the particle, p is the momentum measured by the CDC, γ is $\frac{1}{1-(v/c)^2}$ and v is the velocity measured by the PID detectors. The TOP is set at the barrel region while the ARICH is set at forwarding region. There is no PID detector for the backward region because of the large boost from asymmetric energy.

Both the TOP and the ARICH utilize the Cherenkov Effect. When a particle passes through a matter with a velocity faster than the speed of light in that matter, the light will be emitted with the direction of a certain deviated angle θ, which is the Cherenkov Effect. θ obeys the following equation.

$$\cos\theta = \frac{c}{nv} \tag{2.10}$$

where c is the speed of light, n is the refractive index of the interaction medium, and v is the velocity of the particle.

Time of Propagation Detector

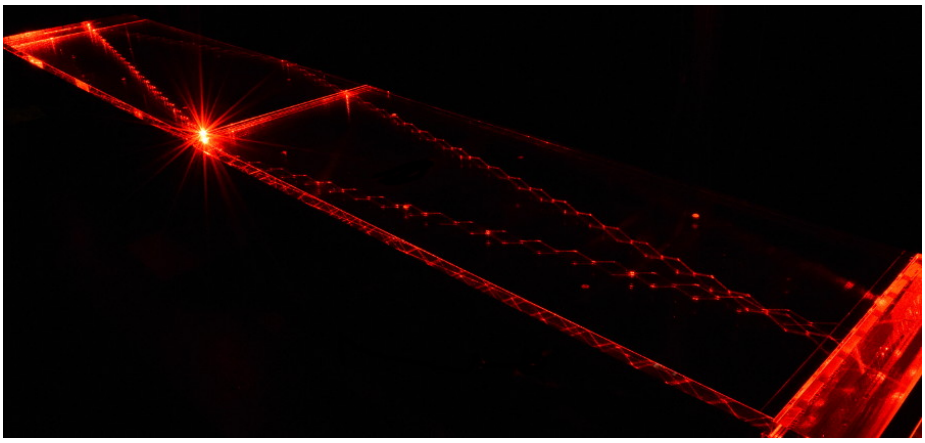

Figure 2.8: Internal reflection of a laser inside one of the 16 bars of TOP [10]

The TOP comprises quartz bars as the medium for the Cherenkov Effect. The radiated Cherenkov photons are totally reflected within the quartz bars as shown in Fig. 2.8. The faster speed brings a larger angle, corresponding to less time propagation time. based on the propagation time, the velocity can be reconstructed.

Aerogel Ring-Imaging Cherenkov Detector

Aerogel is used as the medium in the ARICH. As described by Eq. 2.10, Cherenkov radiation obeys a certain angle from the track of the particle, which results in

a conical propagation. Based on the characteristic radius, the velocity can be reconstructed.

2.4.3 Electromagnetic Calorimeter

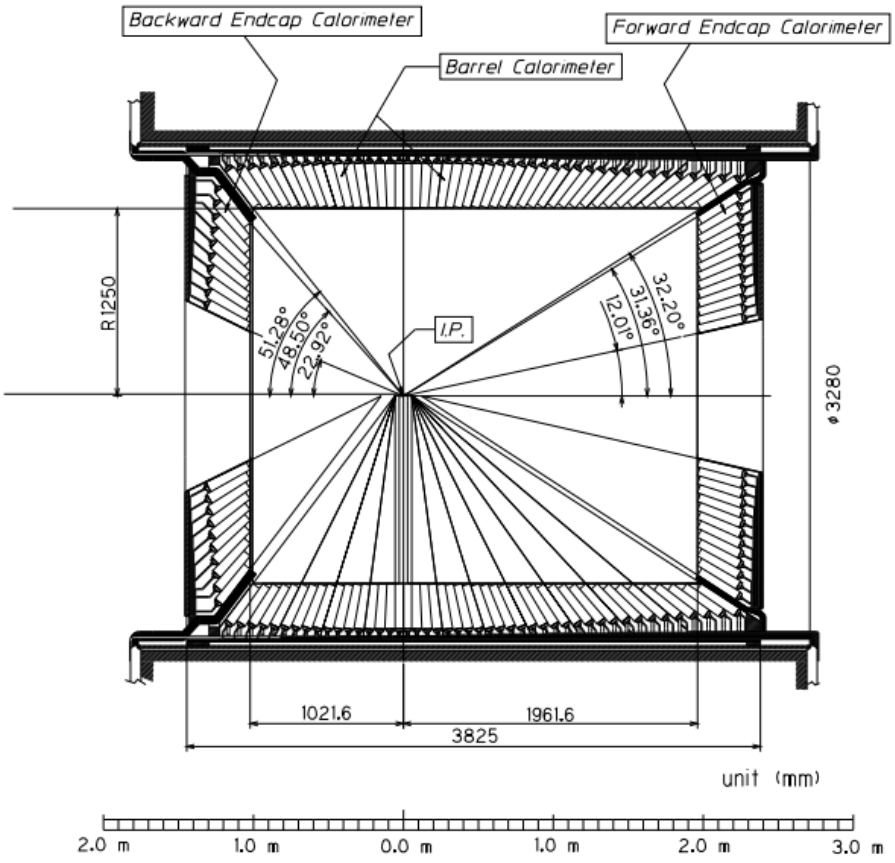

Figure 2.9: The schematic view of the Electromagnetic Calorimeter [13]. The directions of the CsI crystal bars point closely to the IP to precisely measure the polar angle of photons but with a deviation of $1 - 2^\circ$ to fill up the gaps between the CsI crystal bars.

Figure 2.9 shows the schematic view of the Electromagnetic Calorimeter (ECL). The ECL differs from other detectors in that only the ECL can detect photons. Photons and charged particles emit electromagnetic showers by the interaction with Cesium iodide (CsI) crystals. From the deposited energy, the ECL can reconstruct the kinetic energy. Electrons can deposit all its energy in crystals and stop within the ECL while muon can propagate through the ECL and is expected to be captured in the KLM, which can provide further orthogonal information for PID between muon and other charged particles.

2.4.4 Klong and Muon System

K_L^0 is a neutral particle with a long lifetime $c\tau$ of about 15 m, which is longer than the radius of the Belle II detector. Both of K_L and μ have a lifetime long enough to fly through a radius of the Belle II detector. As K_L is a neutral particle that can only interact by hadron reaction and μ is a lepton with much heavier mass than an electron, K_L, μ have a strong penetrability. To detect

these two particles, it is necessary to choose a kind of high-z material as the interaction medium, among which iron is chosen as the interaction medium. The other motive for choosing iron is to prevent the magnetic field in the Belle II detector from leaking into outer space. The Klong and Muon System (KLM) has tens of iron plates with a thickness of about 4.7 cm and an interval of 4.4 cm. To collect the emitted charged particles by the interaction between K_L/μ and the iron plates, There are two kinds of detectors used in the KLM: resistive plate counter (RPC) which is a kind of gas chamber, and scintillators, either of which is set at the intervals between the iron plates.

2.4.5 Data-Acquisition System and the Trigger System

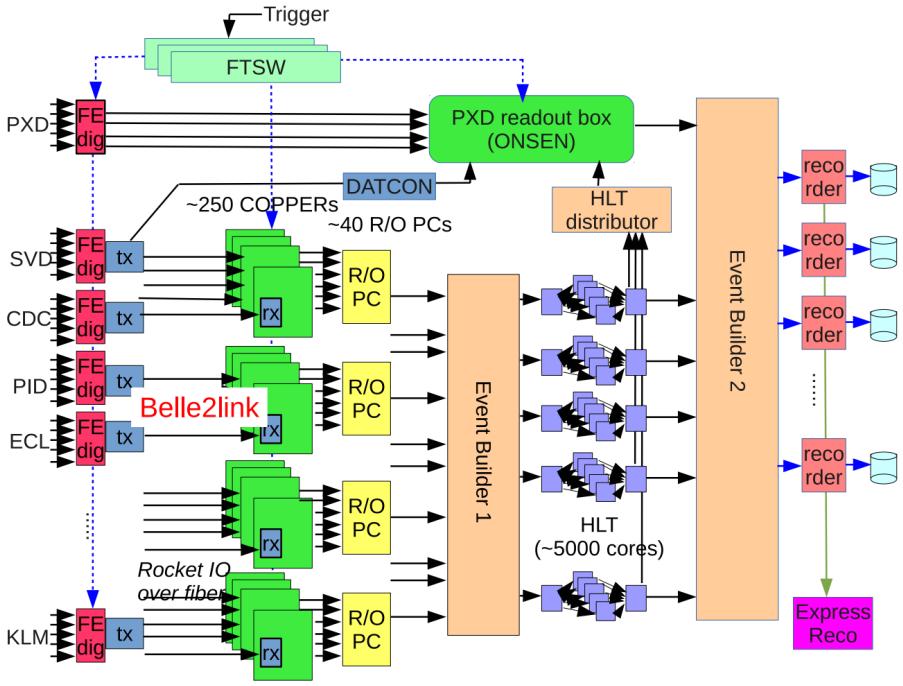

Figure 2.10: Structure of DAQ [14]. The DAQ system is composed of electric circuits very widely from the front-end of each sub-detectors to the back-end recording of data

Figure 2.10 shows the designed structure of the Data-Acquisition System (DAQ). The front ends of each sub-detector are set nearby the corresponding sub-detectors. The digitizers are integrated into the front-ends. The level-1 trigger signal and reset signals at every starting of data acquisition are distributed by a common timing-distribute system called FTSW (front-end timing switch). The digitized data are temporarily saved in the buffers. After the level-1 trigger signal is given, digitized data are sent to the common readout module (COPPER) by a high-rate optical data transformation system (the Belle2link) from the buffers. From more than 200 COPPERs, data are formatted by onboard processors and sent to 40 readout PCs by Gigabit Ethernet (GbE). Events are preliminarily reconstructed on the readout PCs and then fully reconstructed on the High-Level Trigger (HLT) except for the data from PXD. The data flow from the PXD is extremely large, therefore the PXD has a distinct readout system from others. The output data from the HLTs are sent to the PXD readout box that specifies which certain areas of the data are related to the event. This measure can sup-

press the PXD data flow to 1/10 as shown in Table 2.3. The reconstructed events from HLT are further improved by matching with PXD data and then recorded as offline data.

The trigger system in the Belle II is a two-stage pipeline trigger system separated into the Level-1 trigger system and the High-Level Trigger (HLT). The Level-1 trigger preliminarily selects physics event with keeping an efficiency of greater than 99% for $\Upsilon(4S) \to B\bar{B}$ decay mode. Generally, the Level-1 trigger is developed to relieve the load of the DAQ, making the trigger rate smaller than 30 kHz, and the HLT is developed to reduce the size of data storage, reducing the event rate to $1/3 - 1/6$ as shown in Table 2.3. Our study focuses on the Level-1 trigger, so we are to expand the Level-1 trigger detailedly in the next Chapter.

Table 2.3 shows the required performance for the DAQ. For the DAQ, the limit of 30 kHz means ensuring the capability of receiving 30 kHz level-1 trigger signal. As the maximum event size is 1 MB, the maximum level-1 data flow reaches 30 GB/s, which is practically difficult to be totally recorded. To achieve the capability of receiving trigger rate up to 30 kHz, the HLT as one part of the DAQ should discard redundant events and high bandwidths should be ensured between every module shown in Fig. 2.10. By using the reconstructed information until the HLT, we can limit the input region of the PXD and reduce the PXD data to 1/10. Combining the reconstructed information until the HLT and the filtered PXD data, the event is fully reconstructed and recorded with a maximum record rate of 1.8 GB/s.

Table 2.3: Designed performance for the DAQ

	required value
Maximum (level-1) trigger rate	30 kHz
Maximum event size	1 MB
Maximum level-1 data flow	30 GB/s
PXD data reduction rate	1/10
HLT rate reduction rate	$1/3 - 1/6$
Maximum data record rate	1.8 GB/s

2.5 Central Drift Chamber

The Central Drift Chamber (CDC) is one sub-detector in the Belle II, composing the Track System with the PXD and SVD. As the name shows, the CDC is a multi-wire proportional drift chamber. To minimize the multiple scattering, low-Z gas 50% He and 50% C_2H_6 are used in the CDC. Charged particles interact with and ionize the gas, from which the ionized electrons are accelerated by the strong electric field between cathode wires and anode wires and further ionize other atoms, which is called electron avalanche. The electrons in the avalanche are collected by the anode wires and form a current at the front-end electronics. When the voltage established by the current is higher than the preset threshold, it is recorded as a hit in the front-end electronics. The drift time from the ionized location to the anode wires is proportional to the distance to the anode wires, helping more precise measurement of the ionized location. Based on the hits, the CDC can provide information on tracks of charged particles. The cathode wires mentioned above are called field wires and the anode wires mentioned above are called sense wires. To avoid the confusion between the hits mentioned here and the track segment hits introduced in Section 3.3.2, this kind of hit is called "CDC

hit" in this thesis.

Generally, we define the rectangular coordinate system in the CDC as follows. The z direction is the direction of the supposed center-of-mass momentum of an electron and a positron in the two beams. The x directs horizontally and y directs vertically. The order of the directions of the x, y, z obeys the right-handed rule.

There is a uniform magnetic field along the z-direction, the track of charged particles should be a circle or a part of a circle at x-y plane, which is perpendicular to the z-direction. The track complies with $eBr = p$ in the natural unit system where e is the charge unit, B is the magnetic induction intensity, r is the radius of the circle and p is the momentum of the particles. The momentum can be measured by reconstruction of the radius r, which is the main objective of the CDC.

2.5.1 Structure

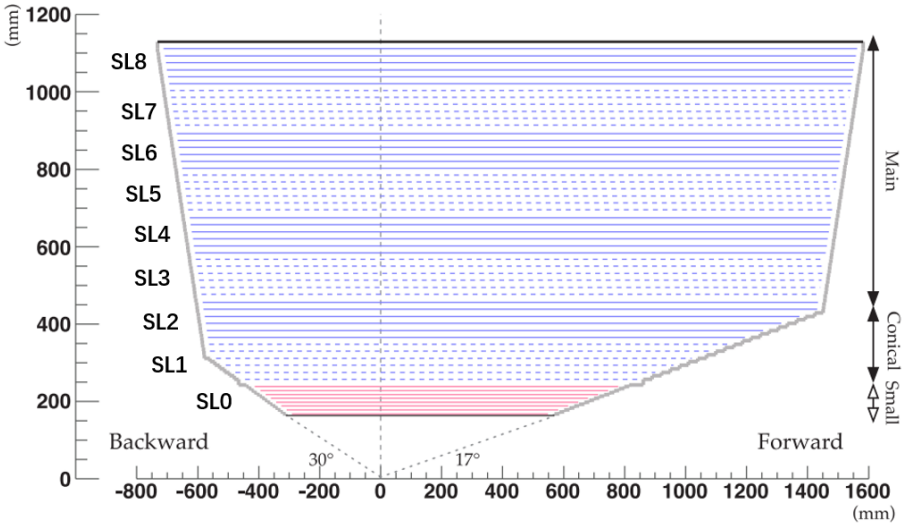

Figure 2.11: Lateral view of the CDC [15]. The solid lines denote axial layers and the dashed lines denote stereo layers whose direction deviates a little from z direction

Fig. 2.11 shows the lateral cross-section view of the CDC. The CDC has 56 layers of sense wires that are basically along the z axis. Every layer has $160-384$ sense wires along the circumference. The farther from IP, the more cells in one layer. The 56 layers are divided into 9 "super layer"s (SL). Every super layer is composed of 6 layers except for the innermost super layer with 8 layers. 5 super layers are axial, in which all wires are axial wires exactly along the z axis to reconstruct the 2-dimensional track (2D track), and 4 super layers are stereo, in which all wires deviate from z axis a little to reconstruct the 3-dimensional track (3D track). Axial super layers and stereo super layers lie alternately from the inner region to the outer region. In Fig. 2.11, the solid lines are the axial layers and the dashed lines are the stereo layers. From inner to outer, The super layers are in sequence denoted as SL0, SL1, SL2, ..., SL8 in this thesis. As the study of this thesis focuses on the 2D track trigger, SL0, SL2, SL4, SL6, and SL8 are mainly utilized in this thesis.

Every "cell" consists of 8 surrounding field wires and 1 sense wire in the center. The cathode field wires are shared by adjacent cells, while the anode sense wires specify and represent the cells. There are 42240 field wires and 14336 sense wires

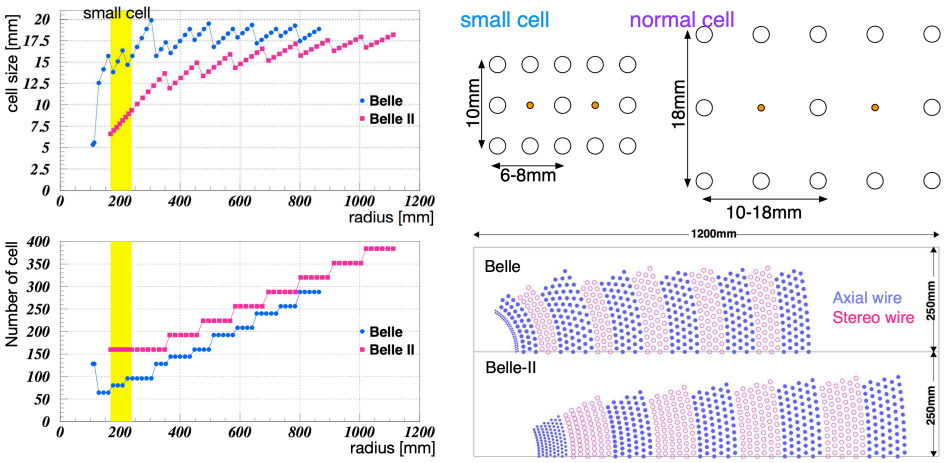

Figure 2.12: The cell size (upper-left), the number of cells (lower-left), and the lateral view (lower-right) along the z direction are shown. The upper-right picture shows the schematic view of small cells and normal cells in which orange points are sense wires and white circles are field wires [15]

(CDC cells) in the CDC. The field wires are made of aluminum with a diameter of 126 μm, and sense wires are made of plated tungsten with a diameter of 30 μm. SL0 utilizes small cells and other super layers utilize normal cells.

To suppress the anticipated increase of the beam background, the size of each cell in Belle II CDC has become smaller than that in Belle CDC as shown in Fig. 2.12. The smaller the size of cells, the shorter the maximum drift time, the narrower the time window, the less influence from the beam background. Because the innermost super layer (SL0) is especially vulnerable to the beam background, the size of the cells in the innermost super layer is about half of that in other super layers. In Belle II CDC, the normal maximum drift time is around 500 ns, while the drift times in inner layers especially in SL0 are shorter due to the smaller cell size as shown in Fig. 2.12.

2.5.2 Readout Module

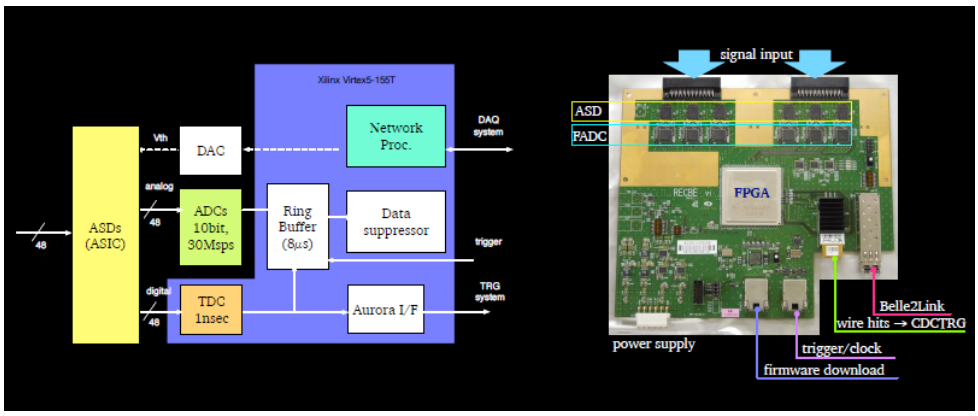

Figure 2.13: Diagram of CDC readout system and photograph of the front-end board for mass production [15]

In the face of 30-fold higher luminosity than the Belle, the readout system is

important to determine the performance of the Belle II CDC. The readout module also includes the digitizers integrated into front-ends close to the backward endplate of the CDC. The ASIC chips, FADC, and FPGA are assembled on a single board. The ASIC chip integrates the amplifier, shaper, and discriminator. The drift time is measured by the Time-to-Digital Converter (TDC) with a resolution of 1 ns. The collected charge that corresponds to the deposited energy is measured by the Analog-to-Digital Converter (ADC). The timing information (TDC) of part of the layers and the map of hits are sent to the CDC trigger. The information of deposited energies (ADC) is not sent to the CDC Trigger.

2.5.3 Origin of Beam Background in CDC

As this study focuses on the track trigger, the effect of the beam background on the CDC is very important.

Fig. 2.14 shows the vertices of particles generating background hits in CDC by the Monto Carlo simulation (MC). The MC utilizes SAD (Strategic Accelerator Design) and GEANT4 (Geometry and Tracking 4). The SAD simulates the beam background in IR (Interaction Region) and the GEANT4 simulates the interaction between beam background particles and the CDC detector. The beam condition was based on May 9, 2020 beam background study condition. Bremsstrahlung radiation was not included assuming that the effect from Coulomb scattering is much higher than that of bremsstrahlung radiation. Figure 2.14 shows the vertex of the mother particles of the simulated CDC hits. The vertices of the photons are in the proximity of the beam while the vertices of the electrons are inside CDC. The energy of the photons are mostly under 1 MeV. It can be reasonably assumed that the shown electrons are actually the secondary electrons from the interaction between the gas particles in the CDC and the low-energy photons, which means that the fundamental source of the background hits is low-energy photons in the proximity of the beam pipe which passes through the VXD. They interact with the gas by effects such as plunk effects or photoelectric effects within CDC and cause beam background hits.

Real data shows that the low-energy photons in the proximity of the beam pipe are not all sources of beam background hits. Non-ignorable amount of charged particles in the beam background reaches CDC, leaving beam background hits from real charged particles instead of photons. However, they did not significantly appear in the above simulation.

From the formulae 2.8 and the formulae 2.9, the magnitude of the single-beam background in LER or HER can be written as $T \cdot \frac{I^2}{n_b \sigma_y} + BI(P_0 + kI) + C$ where T and B respectively denotes the magnitude of Touschek and beam-gas background, P_0 is the base gas pressure and kI is additional gas pressure caused by the beams. T and B are different between LER and HER. As the luminosity background is proportional to the luminosity, it is parameterized as $k_l L + C_l$ where k_l and c_l are parameters and L is the luminosity. At a study for the single-beam background, the hits are recorded at several different beam currents. By using the data of the current and the number of hits, the parameters shown above can be measured. Based on the measured parameters, Figure 2.15 shows the anticipation of CDC hit rates per sense wire (or to say per CDC cell) of each beam background component on 56 layers at the environments of targeted luminosity by extrapolation. The 55th layer was not joined because the 55th layer was masked for malfunction. The average CDC hit rate for a sense wire is about 200 kHz. The luminosity background and beam-gas background will be expected to be 1:1 . LER single-beam background will be much higher than

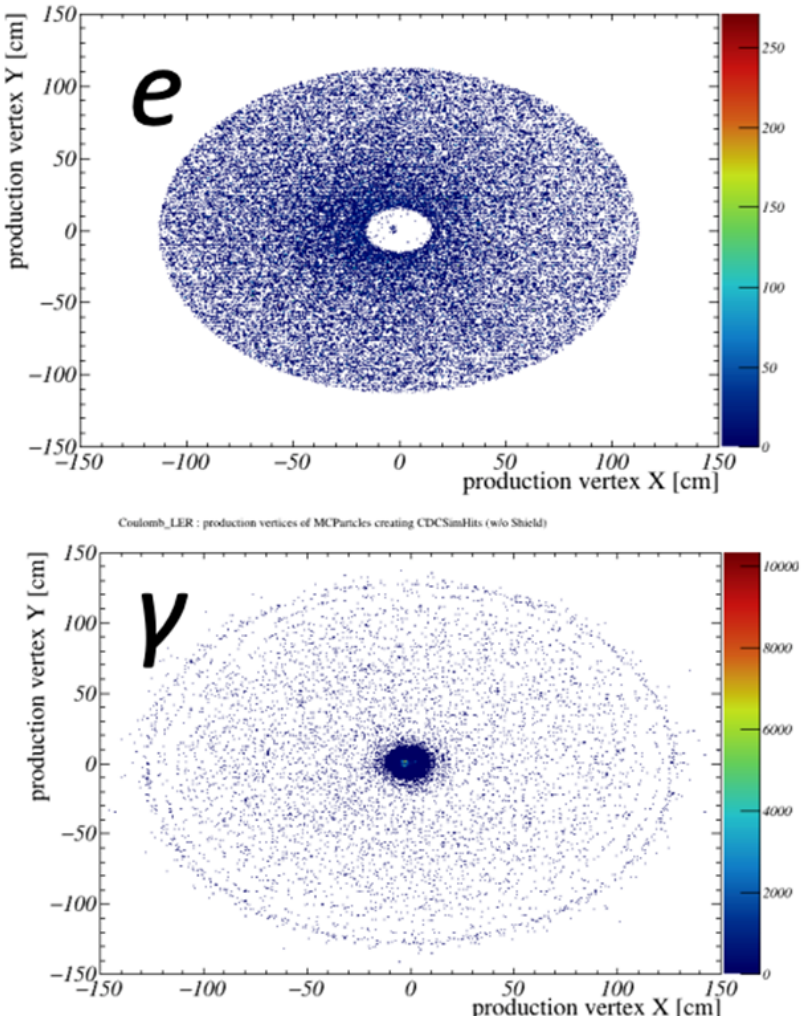

Figure 2.14: The vertex of the mother particles that cause the simulated CDC hits [16]

HER single-beam background, and the beam-gas background will dominate the single-beam background both in LER and HER.

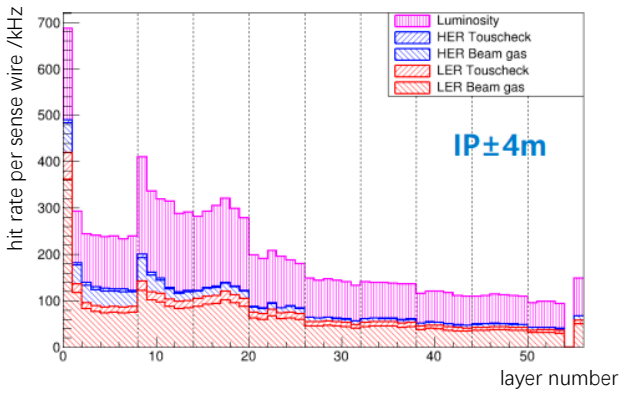

Figure 2.15: Expected CDC hit rates of each beam background component on every layer. The beam background comes from the region near the IP within 4 m [17]

a

Chapter 3

Level-1 trigger System

The Level-1 trigger System is committed to previously selecting physics events especially $\Upsilon(4S) \rightarrow B\bar{B}$. The requirements for the trigger system are as follows [2]:

1. Trigger rate is smaller than 30 kHz.
2. Trigger efficiency for $\Upsilon(4S) \rightarrow B\bar{B}$ decaying events is close to 100%.
3. Fixed latency from the collision is 4.2 μs.
4. Time precision is better than 10 ns.
5. Minimum time interval to separate two events is 400 ns.

The basic structure of the Level-1 trigger is based on that in the Belle, while the majority of the electric circuits are implemented on FPGA to satisfy these requirements by flexible updates of firmwares. At the targeted luminosity, the event rate of physics events is expected to be 15 kHz as shown in Table 3.1. To meet the limit of 30 kHz, the trigger rate caused by the beam background should be smaller than 15 kHz.

Table 3.1: Cross sections of physics events and their rates at the designed luminosity[18]. The rates of Bhabha scattering and $\gamma\gamma$ are estimated with a prescale respectively of 100 and of 10. The rate of the two photon events is estimated from the condition of the Belle.

Process	σ(nb)	Rate(Hz)
$\Upsilon(4S)$	1.2	960
Continuum	2.8	2200
$\mu^+\mu^-$	0.8	640
$\tau^+\tau^-$	0.8	640
Bhabha	44	350 (prescale 100)
$\gamma\gamma$	2.4	19 (prescale 10)
Two photon	12	10000
Total	67	$\sim$ 15000

Brief introductions of the structure of the Level-1 trigger system and the universal boards used in the Level-1 trigger are respectively given in Section 3.1 and Section 3.2. The structure of the CDC Trigger is introduced in Section 3.3. The 2D track trigger is elaborated in Section 3.4.

3.1 Structure

Figure 3.1 shows that the Level-1 trigger has four sub-trigger systems. The four sub-trigger systems are the CDC Trigger, the ECL Trigger, the TOP Trigger, and the KLM Trigger. All of the sub-trigger signals are sent to the Global

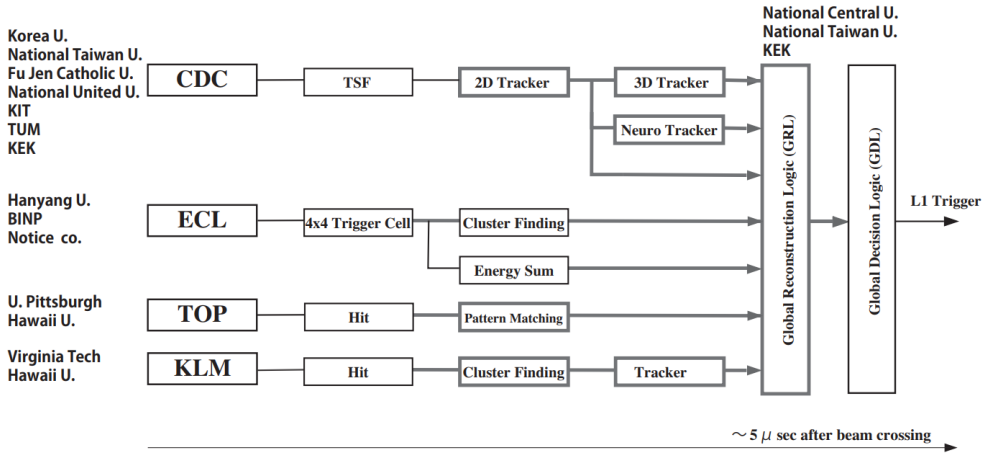

Figure 3.1: The configuration of the Level-1 Trigger[18]

Reconstruction Logic (GRL) and the Global Decision Logic (GDL). The main clock frequency used in the Level-1 trigger is 127 MHz, which is one-fourth of 509 MHz, the RF frequency of the SuperKEKB.

The CDC Trigger measures the number, angle, momentum, charge, and vertex of charged particles, therefore the CDC Trigger is also called "track trigger". The ECL Trigger measures the position, energy, and size of the ECL clusters induced by photons and charged particles. The CDC trigger and the ECL trigger are two main sub-triggers that are able to independently trigger certain events. The TOP Trigger is used to measure the event timing precisely. The KLM Trigger is used to identify muons. The four sub-trigger systems are independent of each other and pipelined in parallel. The GRL is a newly added module in the Belle II Trigger to identify electrons, hadrons, muons, and photons by matching the information from the sub-trigger systems. The GRL is expected to help exclude low-complexity background events. The GDL synchronizes the different latencies of each sub-trigger system and the GRL to send the level-1 trigger signal to the FTSW exactly after 4.2 μs from the beam collision. The level-1 trigger works continuously without any idling time.

3.2 Universal Trigger Board

The electric board used in the BelleII trigger system has been developed. Compared with the Belle, the following features are newly implemented:

1) FPGA has been introduced into the level-1 trigger system. Almost all logic can be updated without changing the hardware boards as long as within the performance limit of each FPGA board.

2) High-speed Serial Communication is used. In the Belle, differential emitter-coupled logic was used as media for data transformation. By changing the communication media, the number of wires between modules can be suppressed to 1/10 with over 100 times higher bandwidth. These protocols of High-speed Serial Communication are used: GTH, GTX, GTY.

"Universal Trigger Board" is developed to realize the above two features. UT3, the 3rd generation of UT was developed in 2012, and UT4, the 4th generation of UT was developed in 2016. Table 3.2 shows the specifications of UT3 and UT4. The first row shows the specified type of FPGA boards. The second row shows the number of logic gates in each FPGA board. The third row shows the bandwidth

of the optical transceivers based on the operating experience. Figure 3.2 shows the photograph of a UT4 board.

Table 3.2: Specifications of the UT3 and UT4. The first row shows the specified types of FPGA boards. The second row shows the number of logic gates in each FPGA board. The third row shows the upper limit of IO that can ensure stability.

	UT3	UT4
FPGA	Xilinx Virtex6 XC6VHX380/560T	Xilinx Virtex Ultrascale XCVU080/160
number of logic cells	382k/580k	975k/2026k
IO	GTH 5Gbps x24lane GTX 3Gps x40lane	GTY 16Gps x32lane GTH 10Gps x32lane

3.3 CDC Trigger System

The CDC Trigger in the Belle only counts the number of charged particles over the threshold of the transverse momentum of 0.2 GeV/c and 0.3 GeV/c, while the CDC Trigger in Belle II also measures the charge, transverse momentum, azimuthal angle of charged particles by 2D track trigger system, and the full momentum, z-position of them by 3D track trigger system. The measurement of z-position is a very strong weapon to exclude the huge single-beam background induced outside IP, mainly concentrating at $z = 0.6\,\mathrm{m}$ as shown in Figure 2.3.

Fig. 3.3 shows the basic configuration of the track trigger. The details of each module are elaborated in the following sub-sections. As my work is on the 2D track trigger, we discuss the 2D track trigger more detailedly in Section 3.4.

3.3.1 CDC Front-end and Merger

The CDC front-end has been introduced in Section 2.5.2. The CDC front-end modules are located at the backward end-plate of the CDC to digitize the timing and charge of CDC hits. As one front-end board is connected to 48 (3 layers of 16 cells along φ direction) sense wires, there are totally of 302 front-end modules. Because the innermost 3 layers are not used in the level-1 trigger, 292 CDC front-ends of them are used for the CDC Trigger.

The front-end modules send the data to the CDC Trigger with a clock frequency of 31.75 MHz, and one-fourth of 127 MHz. The communication from the CDC front-end modules uses 4 channels of GTX and has a bandwidth of 4×2.5 Gbps. "Merger" is used to compress and reform the data from the CDC front-end modules. Every merger board uses 4 front-end modules. The core logic of the merger is detailed as follows.

Figure 3.4 shows an example of one CDC front-end that covers part of the 3^{rd} layer to the 5^{th} layer in the SL0 to explain the logic and function of the Merger. The cells with the number of $0-15$ are the first priority cells. The cells with the number of $16-31$ are the second priority cells. The transferred data are listed as follows. The concepts of track segments, first priority cells and the second priority cells are introduced in the next section. The hit-map means an array of the registers in which the n^{th} register is '1' when the n^{th} CDC cell is hit and is '0' when the n^{th} CDC cell is not hit.

1) the hit-map: 1 bit/cell$\times$32 cells=32 bits

2) the timing of the priority hit for each track segment: 5 bit/cell$\times$16 cells=80 bits

Figure 3.2: The photograph of UT4.

3) second priority cell flag showing whether the priority hit is the second priority cells: 1 bit/cell × 16 cells = 16 bits

4) fastest hit timing among cells in each track segment (TS): 1 bit/TS × 16 TSs = 16 bits

5) edge information: hit timing of cell 31: 5 bit/cell × 1 cells = 5 bits

6) clock counter: 9 bits

7) check sum (XOR of all odd bits and event hits): 2 bits

The 4) is needed for the reconstruction of event timing. 2) and 4) are needed for reconstructing the event timing. The 5) is recorded in case the cell 31 becomes the second priority cell of the adjacent track segment.

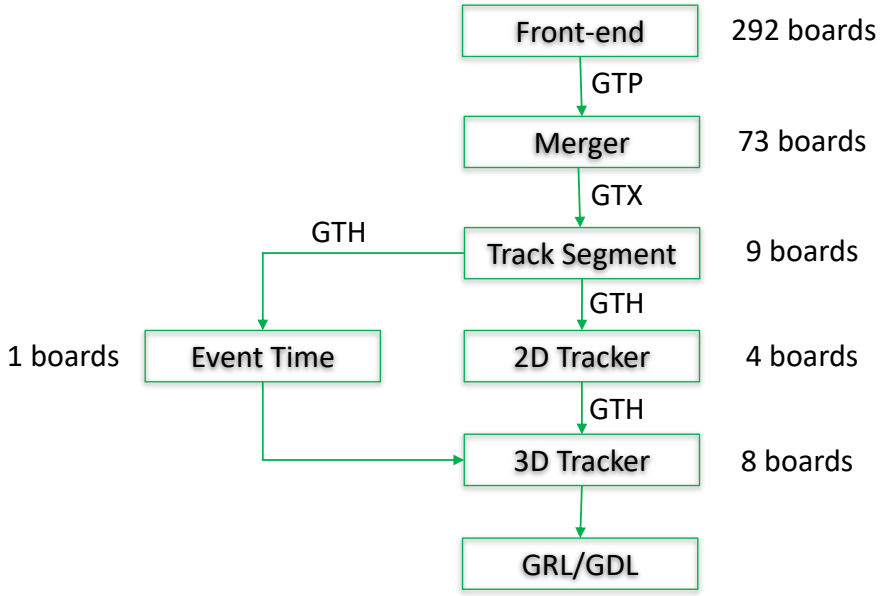

Figure 3.3: Data flow and modules of the CDC Trigger. The words beside the arrows show the protocol of the high-speed serial communication. The merger uses Artex serial FPGA boards and other modules use Xilinx, serial FPGA boards.

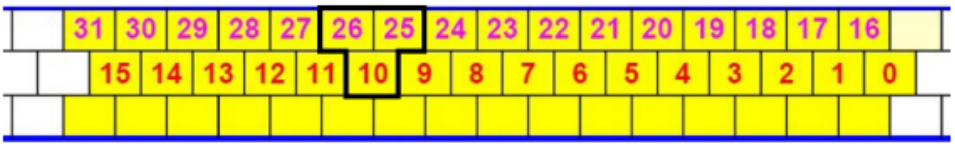

Figure 3.4: An example of a CDC front-end [19]. The yellow squares are the CDC cells whose hit information is processed by the front-end module in this example. Every front-end module uses 3 layers of 16 cells along φ direction. This examples shows part of the 3^{rd} layer to 5^{th} layer within SL0, where the 3^{rd} layer is not used in the CDC Trigger.

3.3.2 Track Segment Finder

By using the CDC hit-map from the merger, "Track Segment hits" are formed by the track segment finder modules. The shape of the track segments on SL0 is different from that on other super layers because of the higher background in the inner layers, which are shown in Fig. 3.5. Five layers in every super layer are used to form track segments. The track segments on SL0 use the fourth to the eighth layers from the inner to outer, while the track segments on other super layers use the first to the fifth layers from the inner to outer. The innermost 3 layers on SL0 and the 6th layer of every other super layer are not used in the track trigger. The total number of track segments is 2336. Note that the adjacent track segments only shift by one cell, thus sharing 10 (6) same cells with each other if they are at SL0 (super layers except SL0).

A track segment hit is formed when at least four layers out of the five layers

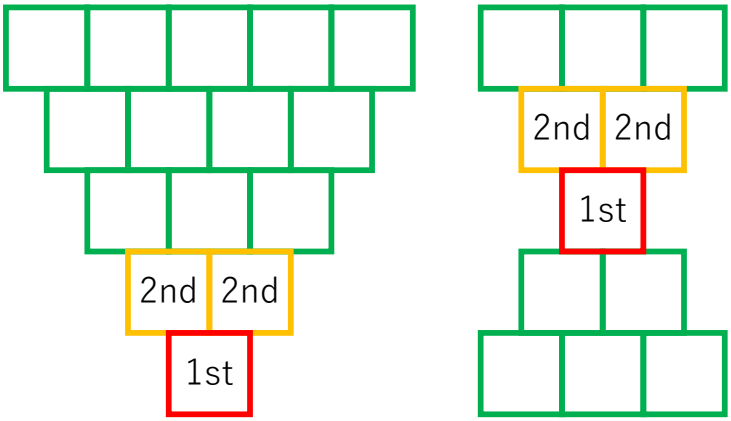

Figure 3.5: Track Segment on SL0 (left) and other SLs (right). Every square represents one CDC cell. The red cell is the first priority cell of the track segment and the two orange cells are the second priority cells of the track segment.

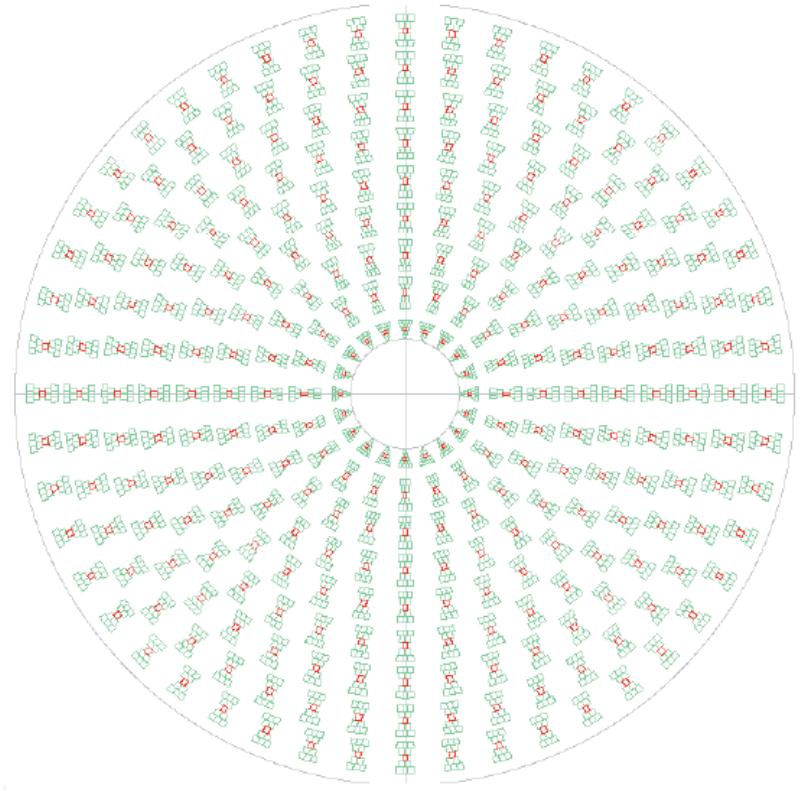

Figure 3.6: Cross section of CDC represented by Track Segment (only 1/8 of all Track Segments shown) [18].

have CDC hits in the track segment.

The red squares shown in Fig. 3.5 is the first priority cell. The cell at the upper-left of the first priority cell is left secondary priority cell, and the cell at the upper-right of the first priority cell is right secondary priority cell. If the first priority cell is hit, it represents the track segment hit as the "priority hit". If the first priority cell is not hit, while the left secondary priority cell is hit, the left secondary priority represents the track segment as the "priority hit". If both the first and left secondary priority are not hit, while right secondary priority cell is hit, right secondary priority cell represents the track segment as the "priority hit". Every track segment hit should have at least one priority hit. The position and the timing information of a track segment hit in the algorithms are assumed to be that of the priority hits.

Track segment is designed to reconstruct charged particles with a transverse momentum larger than 0.3 GeV. If the transverse momentum of a charged particle is lower than 0.3 GeV, track segment hits can hardly be formed at outer super layers especially for SL8, because the injection angle deviates largely from the normal of the track segments.

3.3.3 Trackers and Event Timing

The 2D tracker module uses a technique called "Hough Transformation". As an advantage of the collision experiments, one degree of freedom is reduced because we assume the particles should originate from the IP. The track of a charged particle is assumed to be a circle (by the 1.5 T magnetic field) from the IP. As a result, only 2 independent parameters are needed to determine a 2-dimensional track (2D track). The hough transformation extracts two essential parameters (the direction of initial momentum at the IP and the reciprocal of the radius) to determine the 2D track of particles with axial track segment hits. The detailed techniques are elaborated at the next chapter.

The "Event Timing Finder (ETF)" measures the event timing that is necessary for measuring the drift time used in the reconstruction of 3D tracks and the "Level-1 timing". To keep the independence between each sub-trigger system, it was not adopted to take the event timing directly from other sub-trigger systems. The timing information of the earliest hit in each track segment hit is recorded. The median of them is assumed to be the event timing. To suppress the influence of beam background, only the track segment hits that are related to the reconstructed 2D tracks are taken into the measurement.

3-dimensional tracks (3D tracks) are reconstructed with 2D tracks and track segment hits in the stereo layers. The 3D track trigger finds the adjacent stereo track segment hits besides the track segment hits of the reconstructed 2D tracks. As the distance of the stereo track segment hits from the IP changes along z-axis and can be estimated by the two adjacent axial track segment hits, the z position of this stereo track segment hit can be measured. Based on such information, the z-component momentum of the particle P_z and the z position of the vertex Δz can be measured. P_z and Δz are transferred to the GRL to provide information for matching with other sub-trigger systems and to the GDL to help measurements such as the track counting and the opening angle.

3.4 2D Track Trigger

We discuss the basic logic of the 2D track trigger and the firmware logic of the 2D track trigger in this section.

3.4.1 Hough Transformation in 2D Track Trigger

Hough Transformation is a technique to extract certain features of a shape. To give an example, the formula of a straight line is ordinarily defined as $y = k \cdot x + b$. k and b are two parameters that can define the straight line. If we know one point (x_0, y_0) on the straight line, a relation: $b = y_0 - x_0 k$ is established. If we take b and k as axes of rectangular coordinate (parameter space), the possible combination of the parameters defining the straight line also forms a line, as shown in Fig. 3.7.

A known point on the straight line can exert one relation between the two parameters, which can be shown as a line in parameter space. Therefore, if we know two or more points on the straight line, the intersection of the corresponding lines (possible combinations of parameters) are the true parameter that defines the straight line. Such a technique is called "Hough Transformation".

In experiments, all the measured physical quantities are accompanied by error. In the above example, we only need two points to calculate the parameters of the straight line, and the other points are redundant from the ideal mathematical view. While in reality, the intersections of more than 3 lines cannot be exactly just one point due to error. The more points we have measured, the more intersections we will get in parameter space. The mean value of the intersections is more exact than the true value, which is the reason why hough transformation is applied in physics experiments.

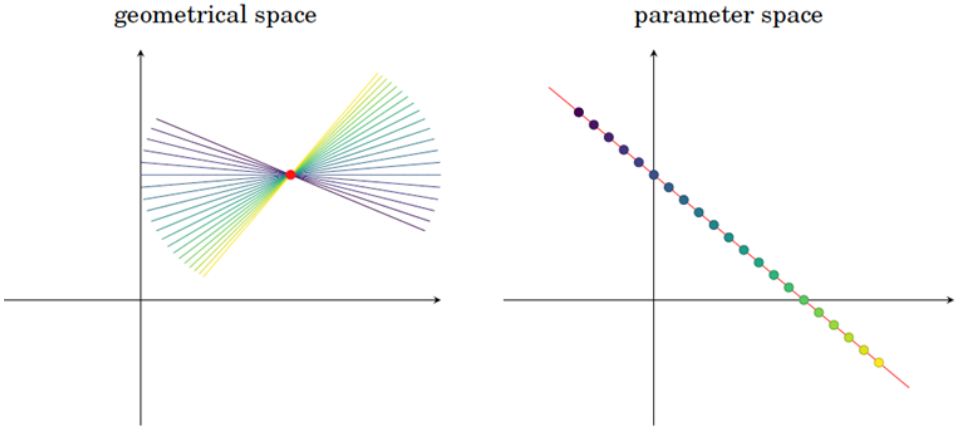

Figure 3.7: The left picture shows the straight lines and the right picture shows the corresponding points with the same color in the parameter space of k and b [20]

In the Belle II, a 1.5 T uniform magnetic field along the z-axis is exerted within the detectors except for KLM. Therefore, in the x-y plane, the track can be thought of as a part of a circle from the IP (interaction point). To define a circle in the 2D plane passing through the origin point corresponding to the beam pipe, we need 2 independent parameters. They can be, for example, the x-y position of the center of the circle (x_c, y_c) or the initial direction on the x-y plane and the radius of the circle. A similar form to the latter one is actually selected in the 2D track trigger, which is to be introduced in the following.

In an ordinary x-y plane polar coordinate where the origin point corresponds to the z-axis, the radius of the track/circle is denoted as r and the azimuthal angle of the center of the circle is denoted as φ. We can derive

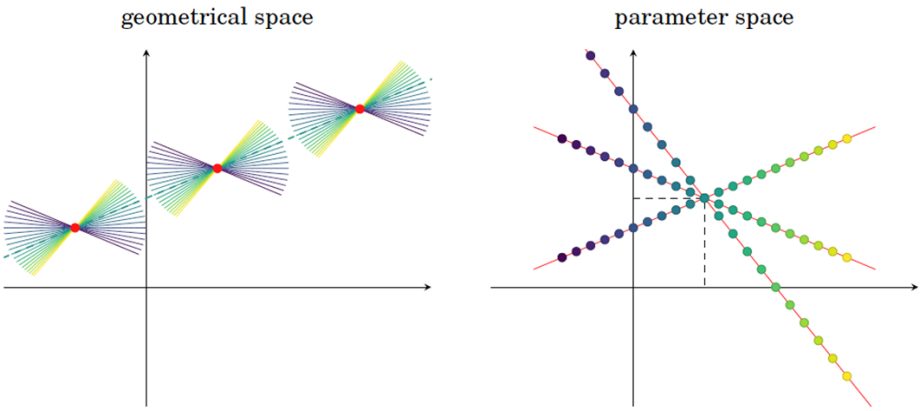

Figure 3.8: The left picture shows the possible straight lines that pass through each red point and the right picture shows the corresponding points of them with the same color. The intersection of the 3 lines (3 sets of possible combinations for each red point) describes the straight line that passes through all the 3 red points [20].

Table 3.3: The r_{TS} of the first priority cells and the second priority cells and the number of cells at each layer of SL0, SL2, SL4, SL6, and SL8.

	r_{TS} of the 1st priority cell /cm	r_{TS} of the 2nd priority cell /cm	the number of cells at every layer N_c
SL0	19.80	20.80	160
SL2	40.16	41.98	192
SL4	62.00	63.82	256
SL6	83.84	85.66	320
SL8	105.68	107.50	384

$$\begin{aligned} r^2 &= (x - r\cdot\cos\varphi)^2 + (y - r\cdot\sin\varphi)^2 \\ 0 &= x^2 + y^2 - 2r\cdot(x\cdot\cos\varphi + y\cdot\sin\varphi) \\ \frac{1}{r} &= \frac{2x}{x^2+y^2}\cdot\cos\varphi + \frac{2y}{x^2+y^2}\cdot\sin\varphi \end{aligned} \tag{3.1}$$

Here, we take x' as $\frac{2x}{x^2+y^2}$ and y' as $\frac{2y}{x^2+y^2}$. x' and y' have a linear relation, which means that the circle/track becomes into a straight line by such transformation as shown in Fig. 3.9. (x, y) can be substituted by the position of the track segment hits. r_{TS} and φ_{TS} denote the position of the priority hit of the track segment hit at the polar coordinate of x-y plane. φ_{TS} is calculated by the track segment ID. We denote N_c as the number of cells at each layer within a super layer. The track segment ID at each super layer has a range from 0 to $N_c - 1$. If the priority hit is the first priority cell, the track segment ID '0' corresponds to a φ_{TS} of '0', and the track segment ID 'n' corresponds to a φ_{TS} of $n\frac{2\pi}{N_c}$. Because the adjacent layers within one super layer is staggered as shown in the shape of track segments, the φ_{TS} of the left (right) second priority cell is the $n\frac{2\pi}{N_c} + (-)\frac{\pi}{N_c}$ for the track segment ID 'n'. Table 3.3 shows the detailed r_{TS} and N_c. φ_0 is defined as $\varphi + \pi/2$, which is actually the azimuthal angle of initial momentum with some assumptions shown by the later deduction. We can derive

$$\begin{aligned}
\frac{1}{r} &= \frac{2\cos\varphi_{TS}}{r_{TS}} \cdot \cos\varphi + \frac{2\sin\varphi_{TS}}{r_{TS}} \cdot \sin\varphi \\
\frac{1}{r} &= \frac{2}{r_{TS}} \cdot \cos(\varphi_{TS} - \varphi) \\
\frac{1}{r} &= \frac{2}{r_{TS}} \cdot \sin(\varphi_0 - \varphi_{TS})
\end{aligned} \tag{3.2}$$

Here, we take φ_0 and $1/r$ as the two parameters defining the track/circle.

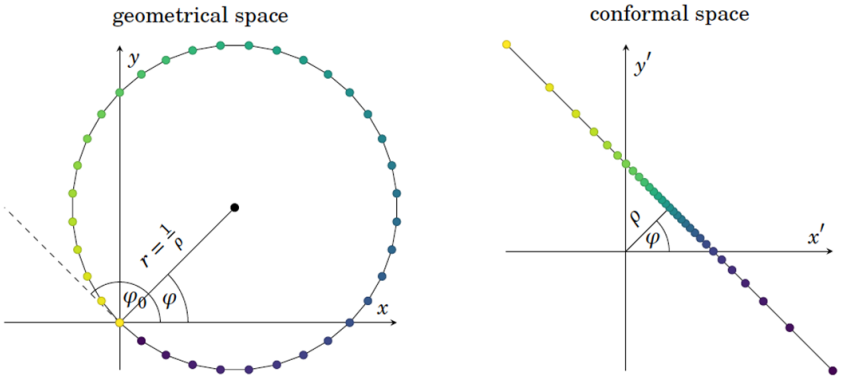

Figure 3.9: The left picture shows a circle passing through the origin point and the right picture shows that it is reshaped to a straight line in the conformal space of x' and y' [20].

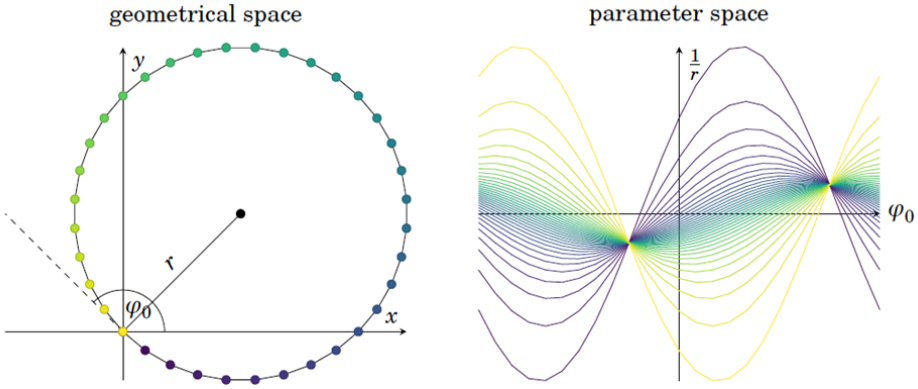

Figure 3.10: The left picture shows a circle passing through the origin points with several points with color. Each curve in the right picture represents the set of the parameters of all possible circle that passes through the point in the left picture with the same color and the origin point. The intersection of these curves in the right picture describes the circle that passes through all colored points in the left picture [20].

Figure 3.10 shows the corresponding curve of the points on the curve. Though $1/r$ physically cannot be minus, we assume it to be free mathematically by defining the minus radius to be a central symmetry circle. By this assumption, we can get two intersections of the curves that point to the same circle without a limit on the range of φ_0. The $1/r$ of the two intersections are opposite, and the interval between φ_0 is 180°.

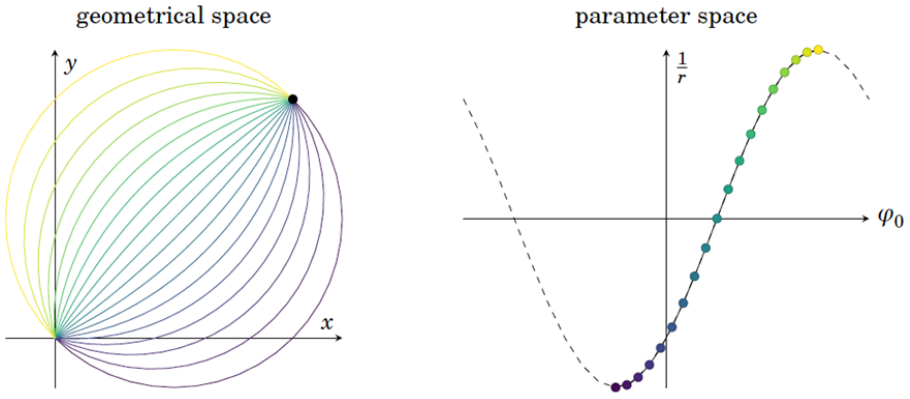

Figure 3.11: The right picture shows one curve with colored points in the parameter space, corresponding to the black point (hit) in the left picture. The left picture shows the corresponding semicircles (tracks) of the points with the same color on the curve in the right picture. [20]

Practically, we limit the range of φ_0 to be between $\varphi_0 - 90°$ and $\varphi_0 + 90°$ for the function 3.2. By this way, we can know that

$$\frac{d(1/r)}{d\varphi_0} = \frac{2}{r_{TS}} \times \cos(\varphi_0 - \varphi_{TS}) > 0. \tag{3.3}$$

By the limitation on φ_0, the function is always an increasing function. The following contents assume the particle has enough momentum to pass through CDC without flying back to z axis. If the φ_0 of the intersection on the curve is between 0° and $\varphi_{TS} + 90°$ (between $\varphi_{TS} - 90°$ and 0°), the following facts can be deduced:

1) The $1/r$ of the intersection is positive (negative), which is one advantage of the limitation on φ_0.

2) The track should be clockwise (anti-clockwise).

3) The particle has a positive (negative) charge.

4) The Initial direction of the momentum at the IP is at the anti-clockwise (clockwise) side of the center of the track/circle.

As to 4), when the $1/r$ is positive, the initial azimuthal angle of the momentum at the IP is $\varphi + 90° = \varphi_0$ as the initial definition of φ is the azimuthal angle of the center of the track/circle. When the $1/r$ is negative, φ_0 is equivalent to $\varphi_0 - 180°$ at the initial physical definition. In this case, the initial azimuthal angle of the momentum at the IP should be $\varphi - 90° + 180° = \varphi_0$. Therefore, φ_0 can always denote the initial azimuthal angle of the momentum at the IP without relation to the charge, which is the other advantage of the limitation on φ_0.

In the 2D track trigger, every axial track segment hit participates in the hough transformation. It is impractical and unnecessary to calculate all intersections. We divide the parameter space into grids like Fig. 3.12. The z-value represented by the color of the hough plane is defined as the number of curves from different super layers passing through it. In the real algorithm, the number of bins of the φ_0 ($1/r$) axis is 160 (34).

Note that track segment hits from the same super layer are not repeatedly counted in one cell because such track segment hits are often adjacent and describe the same part of the track. So the maximum z-value is 5, the number of axial super layers.

The higher the z-value for a cell, the more possible is for the cell to be the

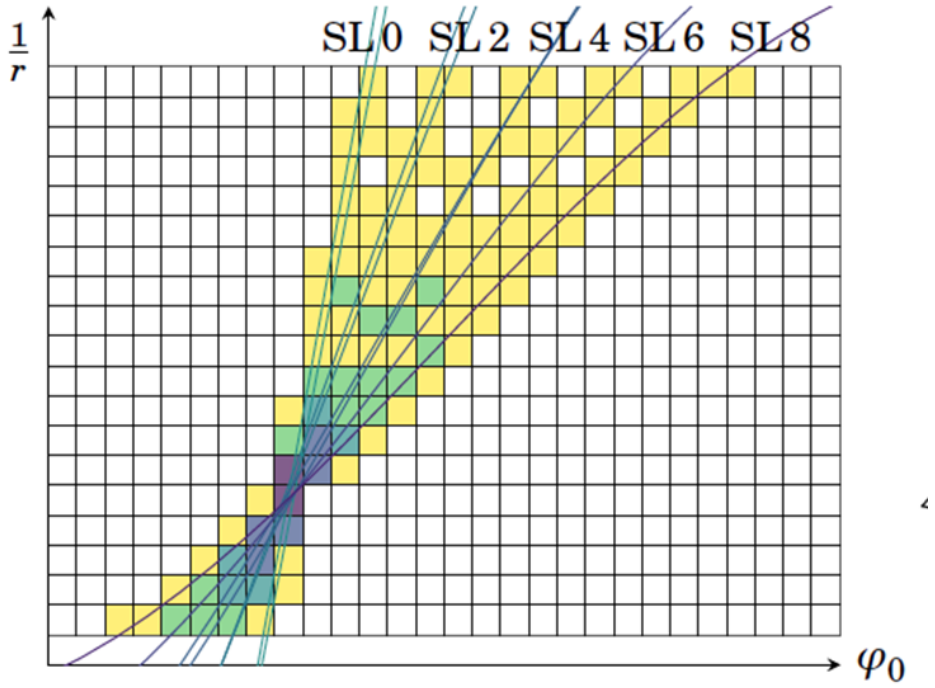

Figure 3.12: Experimentally the hough parameter space is binned as a hough grid. The curves correspond to the track segment hits by Eq. 3.2. In this example, The z-value of each cell in this hough grid is represented by the colors and defined by the number of curves from different super layers that pass through the cell. Yellow is 1, green is 2, blue is 3, deep blue is 4 and purple is 5. The slope of the curve tends to be smaller for the track segment hits from outer super layers [20].

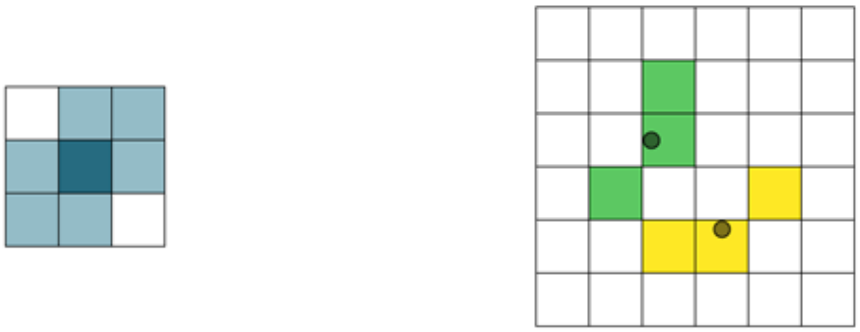

Figure 3.13: The left picture shows the 6 adjacent cells in which the peak candidates can be assimilated into one cluster. The right picture gives an example, in which colored squares are peak candidates and are separated into two clusters. The point in each cluster is the mean position of the member peak candidates in the cluster [20].

intersection describing the true track. The cells whose z-value is higher than a threshold are defined as peak candidate cell. The default threshold in the real algorithm is set as 4, which means that at least 4 track segment hits are required for one track. Like Fig. 3.12, the number of peak candidate for one intersection may well more than 1. It is necessary to cluster the adjacent peak candidates to avoid reconstructing "clone tracks".

An adjacent peak candidate can be at 8 directions. As mentioned before, the curve is always an increasing function. Accordingly, except for top-left and down-right, adjacent peak candidates of other patterns are assimilated into one cluster. Every cluster that has at least two peak candidates is considered to be the reconstructed 2D track. For example, in Fig. 3.13, the six peak candidates are combined into two clusters. Every one cluster represents one reconstructed 2D track.

3.4.2 Firmware logic of the 2D Track Trigger

Fig. 3.14 shows the main configuration of the 2D track trigger in the firmware.

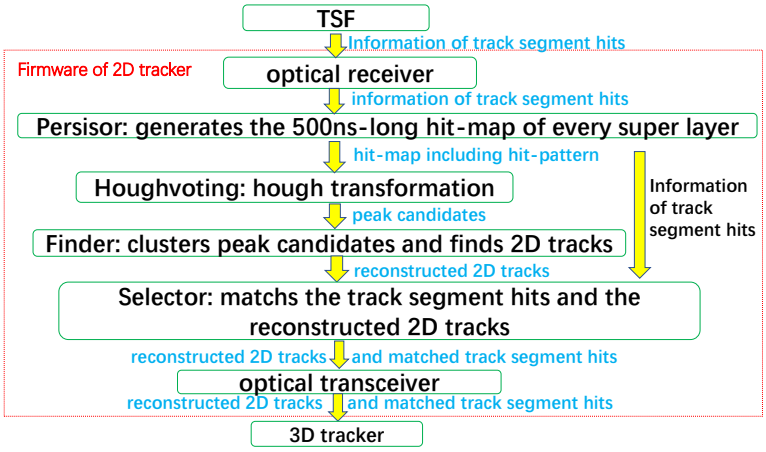

Figure 3.14: The configuration of the 2D track trigger

The track segment finder (TSF) modules as the input for the 2D tracker modules have 9 boards. Each TSF board finds track segment hits in one super layer and the super layer number is added to the name as a suffix. For example, TSF2 is the TSF board that finds the track segment hits in the SL2.

The 2D track trigger receives the input data from TSF modules by optical receivers which are shown in Fig 3.15 and sends the output data to 3D tracker modules by optical transceivers. The maximum number of track segment hits in a clock of 32 ns is 15 due to the limit of the bandwidth. Among the transferred contents shown in the right part of Fig 3.15, only track segment IDs and priority flags are used in the 2D track trigger, while other contents are also received to be transferred to 3D tracker modules.

Figure 3.16 shows the data flow of the data processing in the 2D tracker module. The "Persistor" module generates the hit-array of every super layer based on the track segment IDs. For example, the 123rd register of the hit-array of SL2 is "1" if the track segment ID of a track segment hit from SL2 is 122 as the track segment ID counts from 0. As the maximum drift time of CDC is around

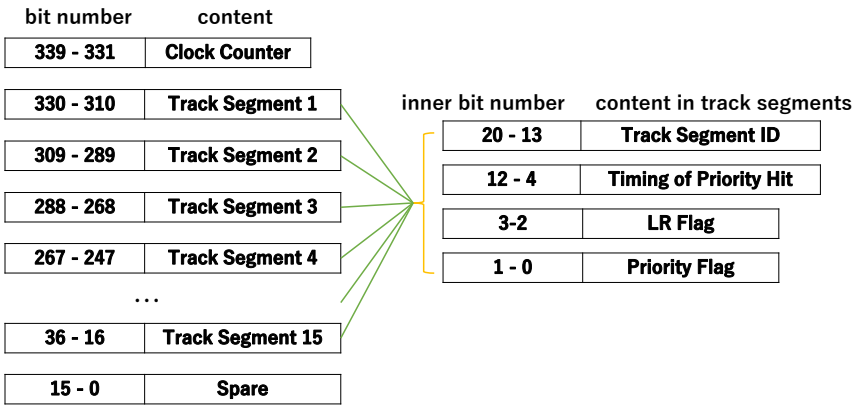

Figure 3.15: The bit-map from TSF modules to 2D tracker modules. The right part shows the transferred information inside each track segment shown on left. The track segment ID is determined by the location of the first priority cell in the layer. The LR flag reflects the tendency to left or right determined by the hit-pattern. The priority flag shows which priority cell is the priority hit of the track segment hit.

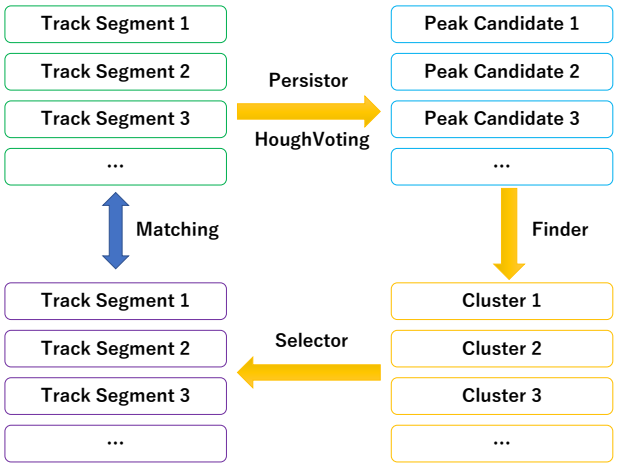

Figure 3.16: The schematic diagram of the data flow in the 2D tracker module

500 ns, around 16 times 32 ns, persistor piles up the hit-array in every clock of 32 ns onto a 16-clock-long hit-array by using first in first out (FIFO).

The “Processor” module takes on two main processing modules: finder and selector.

The “Finder” module maps the hit-map to the hough grid in each super layer by the sub-module ”Houghvoting”. The track segment hits from the same super layer are not repeatedly counted. To realize the logic, the Houghvoting does parallel hough transformation of each axial super layer. The five hough grids from the five axial super layers are merged into one hough grid with judging the peak candidates at the same time. To determine whether a certain cell is a

peak candidate, the number of "1" is counted for the same cell at the five hough grids. If the number of "1" is more than or equivalent to the threshold, the cell is deemed as peak candidate. The default value of the threshold is four as mentioned in Section 3.4.1. The Finder combines the peak candidates into clusters. The clusters with more than 1 peak candidate represent the reconstructed 2D tracks.

The "Selector" module compares the track segment hits and the reconstructed 2D tracks to find out the best fitted track segment hits of every reconstructed 2D tracks. The Selector uses the reverse hough mapping that maps peak candidates to the corresponding track segment hits. By matching the reversely inferred track segment hits and the real track segment hits, the best fitted ones are selected.in

Chapter 4

Performance Evaluation of the 2D Track Trigger

With the future high luminosity environment, performance degradation of the 2D track trigger is expected due to luminosity and beam background. The high beam background makes the 2D track trigger wrongly reconstruct tracks. Some of the tracks are related to the real charged particles, which are called ghost tracks. Some other tracks are repeatedly reconstructed for one charge particle, which are called clone tracks. The wrongly reconstructed tracks including ghost tracks and clone tracks are called fake tracks. The setting up of the simulation is shown in Section 4.1. The performance evaluation of the reconstruction efficiency, fake track rate, and trigger rate of the conventional 2D track trigger is given in Section 4.2. As an attempt to improve the robustness to the beam background, the performance evaluation of the conventional 2D track trigger with other parameters is conducted and shown in Appendix B.

4.1 Monte Carlo Simulation

As it is difficult to achieve the same environment of the targeted luminosity at present, we have to evaluate the future performance firstly by a simulation of the beam background. We use the technique called Monte Carlo Simulation (MC) which is a widely used technique in experimental physics to simulate a certain environment based on some critical parameters.

In this thesis, the level of the beam background during 2020 is used to be the reference for the beam background. For example, BGx5 means 5 times the magnitude of the beam background during 2020 and therefore causes 5-fold beam background hits in the CDC. We use SAD (Strategic Accelerator Design) to simulate the beam background and the GEANT4 (Geometry and Tracking 4) to simulate the interaction between the beam background particles and the detectors. The beam background during 2020 is simulated with the parameters listed in Table 4.1. As introduced in the next section, the beam background level at the targeted luminosity is estimated to be BGx15.

Table 4.1: parameters of beam background during 2020 in simulation

parameters	value
vertical beta function β_y	3 mm
current of LER I_{LER}	1.2 A
current of HER I_{HER}	1.0 A
Luminosity	$1.06 \times 10^{34}\,\mathrm{cm^{-2}s^{-1}}$
The number of bunches n_b	1576

From Fig. 2.15, we can estimate the hit rate per 1 μs which is the time window in simulation by $\sim 0.2\,\text{hits}/\mu\text{s}/\text{wire} \times 14336\,\text{wires} \times 1\,\mu\text{s}/\text{event} = \sim 3000\,\text{hits}/\text{event}$. By comparison with the number of hits in a time window which is to be shown later, in this thesis it is assumed that the background level at the targeted luminosity is 15 times of the beam background during 2020, which is denoted as "BGx15".

To evaluate the reconstruction efficiency and deliberately provide a chance for clone tracks, we add a single charged particle onto part of the simulations. The parameters of this particle are shown in Table 4.2. We select μ^- as the representative charged particle. In real situations, the percentage of barrel and front-end particles is much higher than that of back-end particles. As the 2D track trigger is designed to reconstruct the charged particles passing through the barrel part of the CDC with a momentum larger than 0.3 GeV and has a better reconstruction efficiency for high-momentum charged particles, a momentum of 0.5 GeV/c is selected to satisfy the targeted range of momentum and deliberately raise the difficulty of successfully reconstructing tracks.A uniform distribution is used for the polar angle and the azimuthal angle. Nevertheless, we set a limit of $60° - 120°$ on the polar angle, which corresponds the barrel part of the CDC. We give a discussion on this limit at the next paragraph.

Table 4.2: parameters of the single charged particle in the simulation

parameters	value
particle type	μ^-
momentum p	0.5 GeV/c
distribution of polar angle	uniformly random within $60° - 120°$
distribution of azimuthal angle	uniformly random within $0° - 360°$

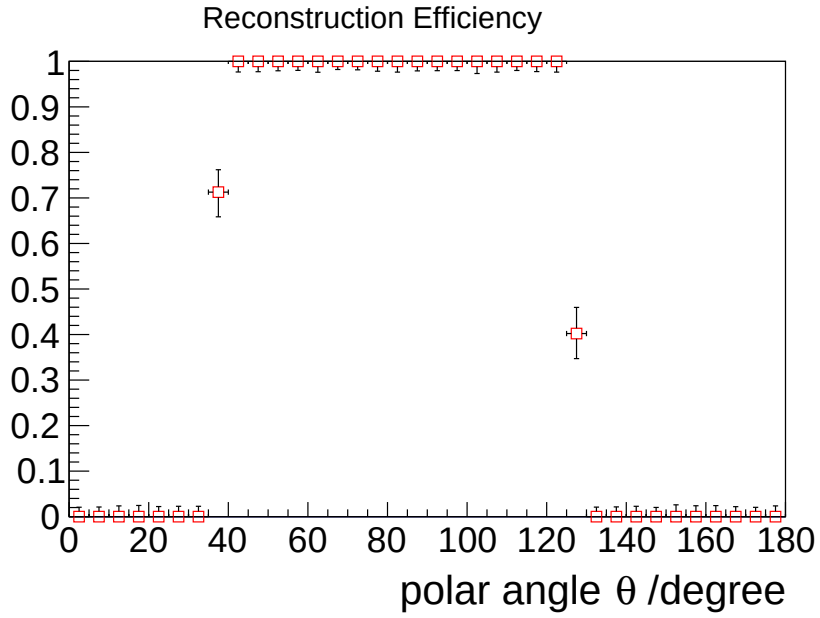

Figure 4.1: The reconstruction efficiency at each range of polar angles. The error bars show statistical errors based on the Clopper-Pearson method.

Figure 4.1 shows the reconstruction efficiency, which is defined as the proportion of simulated events where the simulated muon with the parameters listed in Table 4.2 without the limit on the polar angle is successfully reconstructed. It is

given by the following equation:

$$\text{efficiency} = \frac{N_{track \geq 1}}{N_{all}}, \tag{4.1}$$

where $N_{track \geq 1}$ denotes the number of events in which at least one track is reconstructed and N_{all} denotes the number of all simulated events. This definition of efficiency holds true only when the simulated events only include the simulated muon without beam background. As clone tracks do not occur without simulated beam background, the "at least one track" in the definition is practically the same as "one track".

The reconstruction efficiency outside $40° - 120°$ drops as designed and expected for two reasons. As discussed in Section 3.2, the 2D track requires the charged particle to reach outer layers, at least SL6. While the acceptance of polar angle narrows at outer layers as shown in Fig. 4.2. The coverage at the inner layers is $17° - 150°$, while the coverage at the outermost layer is $35° - 123°$. Another reason resulting in the loss of efficiency for the particles with a small angle to the z-axis is related to the property of the Belle II magnetic field itself, which is detailed in the appendix.

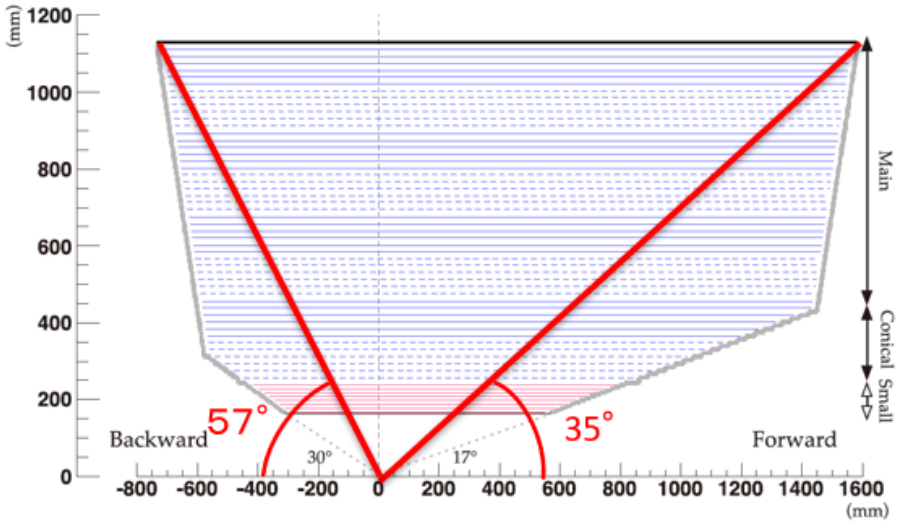

Figure 4.2: The coverage of CDC on polar angles is smaller for the outer layers.

In the simulation, the time window that describes how long time of input data is used in reconstruction is 1 μs, which is double the actual time window 500 ns in the firmware.

4.2 Performance Evaluation of the CDC Trigger at Each Beam Background Level

In the example shown in Fig. 4.3, 4 tracks are reconstructed though only one track is "real" in the simulation of the environment of targeted luminosity. In the corresponding hough grid, some clusters are coincidentally established by beam-background hits and form fake tracks. We discuss in this section the evaluation of the fake track rate, the number of fake tracks, and the trigger rate caused by fake tracks.

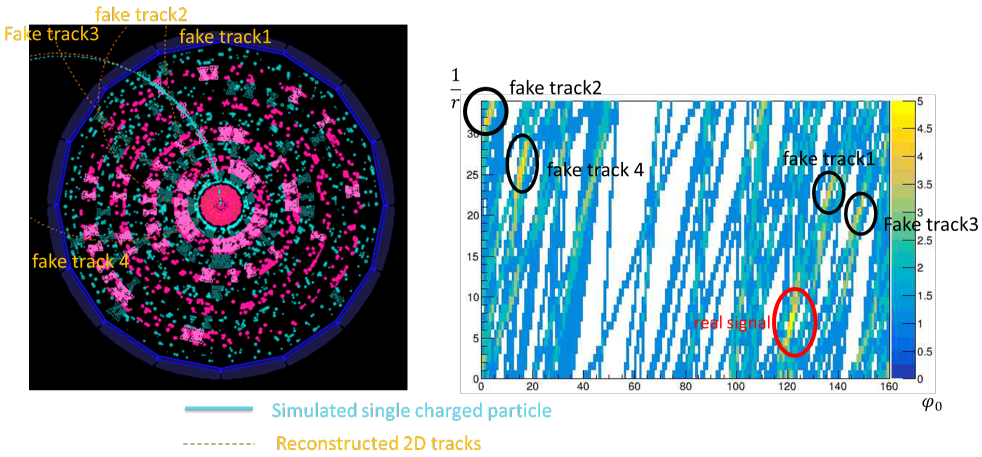

Figure 4.3: An example at BGx20. The orange curves and the blue curve in the left picture respectively denote reconstructed 2D tracks and the simulated muon. The right picture shows the corresponding hough grid.

4.2.1 Number of Beam Background Hits

Fig. 4.4 shows the number of beam background hits in a time window at each beam background level. The number of hits is proportional to the times of the beam background level as expected. As the magnitude of the single-beam background is not definitely proportional to the luminosity, the times of the beam background level is not definitely proportional to the luminosity. We compared Fig. 2.15 and Fig. 4.4 to determine which beam background level can represent the beam background at the targeted luminosity. From Fig. 2.15, an average of 20 kHz hits per sense wire was estimated. As the number of sense wires is 14336 and the time window is 1 μs, we can estimate that the number of hits in a time window is about 3000, which corresponds to BGx15. Therefore, we assume BGx15 to be the beam background level at the targeted luminosity. If we assume that the beam conditions such as n_b, β_y^* introduced in Section 2.3, the beam background level is proportional to the luminosity. With this assumption, the BGx10 corresponds to a luminosity of $4.0 \times 10^{35}\,\mathrm{cm}^{-2}\mathrm{s}^{-1}$ and the BGx20 corresponds to a luminosity of $8.0 \times 10^{35}\,\mathrm{cm}^{-2}\mathrm{s}^{-1}$. As the simulation of beam background is not very accurate, the BGx20 is also simulated.

4.2.2 Number of Fake Tracks

Figure 4.5 shows the number of reconstructed tracks with the simulated muon and each beam background. The purpose to add a simulated muon here is to deliberately provide a chance for clone tracks. As there is one muon in the simulation, the ideal number of reconstructed tracks is one. If the number is 0, the track is not successfully reconstructed. If the number is greater than 1, fake tracks are reconstructed. If the number is 1, we assume that the reconstructed track is the real track of the muon instead of a fake track because the reconstruction efficiency for the muon is practically 100% with a polar angle within $60° - 120°$ as shown in Fig 4.1. Note that the reconstruction efficiency of the muon is not affected by the beam background because the corresponding cluster of the muon in the hough grid does not disappear by the effect of additional beam background hits. Therefore, the number of fake tracks is assumed to be the number of reconstructed tracks minus one. Fake tracks dominate from BGx15 as

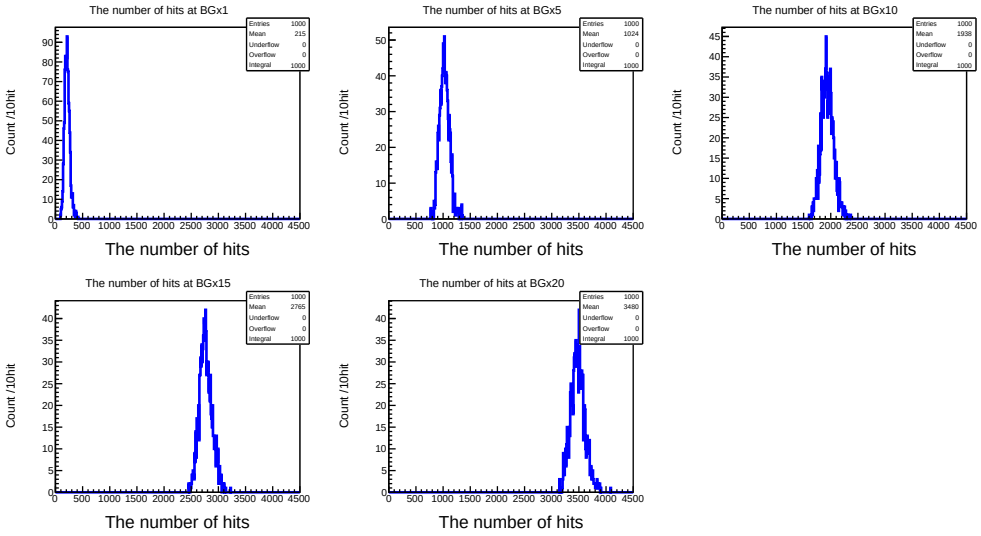

Figure 4.4: The number of beam background hits at each beam background level of BGx1, BGx5, BGx10, BGx15, BGx20

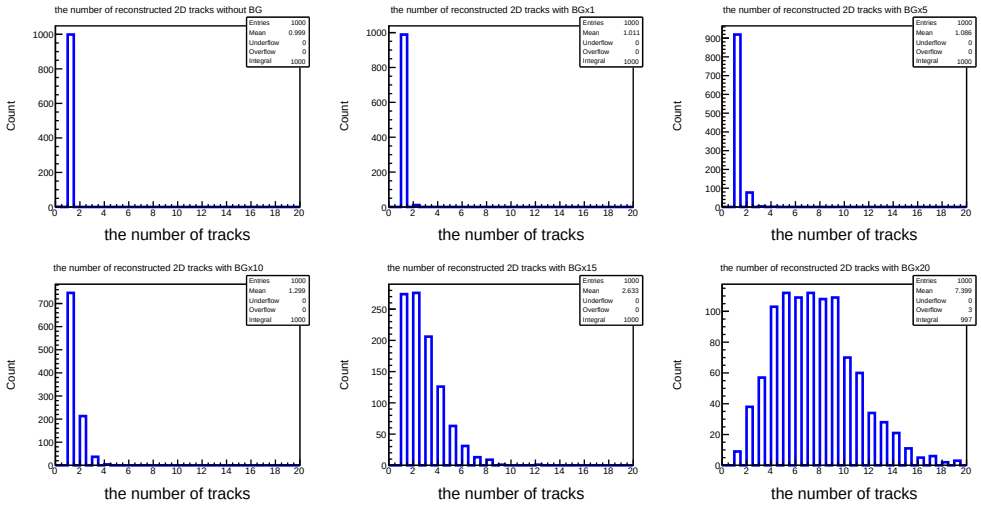

Figure 4.5: The number of reconstructed 2D tracks at each beam background level of BGx0, BGx1, BGx5, BGx10, BGx15, BGx20

shown in Fig 4.5

Fig. 4.6 shows the correlation between the number of hits in a time window and the corresponding number of reconstructed 2D tracks, rendering the number of fake tracks in a different way from Fig. 4.5. The number of fake tracks increases rapidly at a high number of hits. Fake tracks seldom occurs at BGx1, while significantly increases from early phase BGx10 with a number of hits of about 2000 like a switching point.

4.2.3 Fake Track Rate

We define the fake track rate as:

$$\text{fake track rate} = \frac{N_{track>1}}{N_{all}}, \tag{4.2}$$

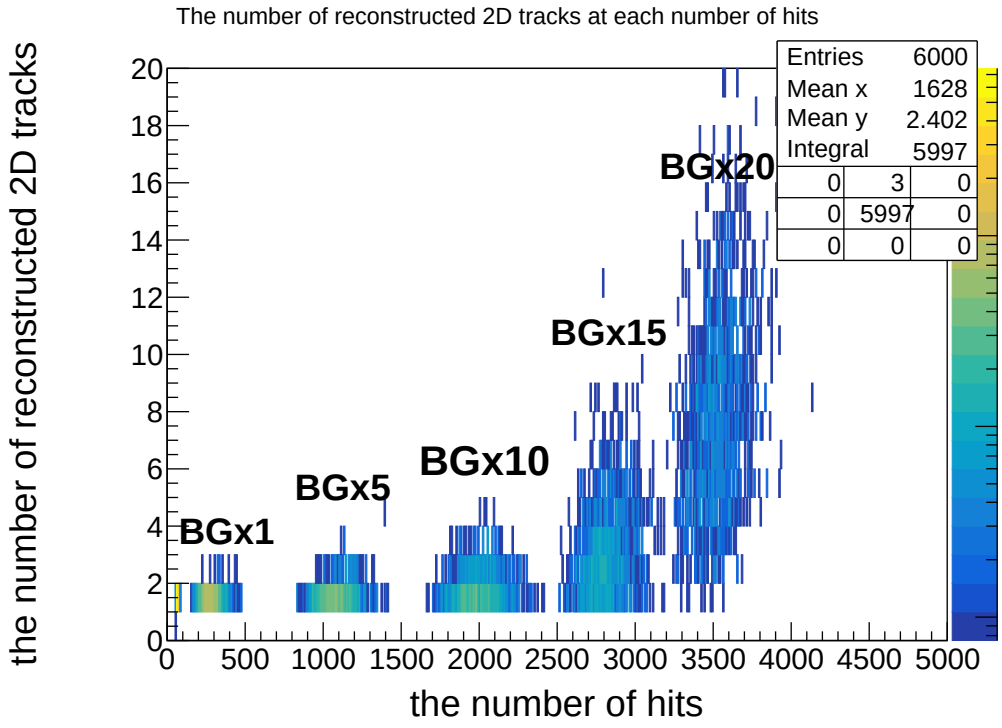

Figure 4.6: The number of reconstructed 2D tracks increases rapidly at a high number of hits.

where $N_{track>1}$ denotes the number of events in which at least two tracks are reconstructed and N_{all} denotes the number of all simulated events.

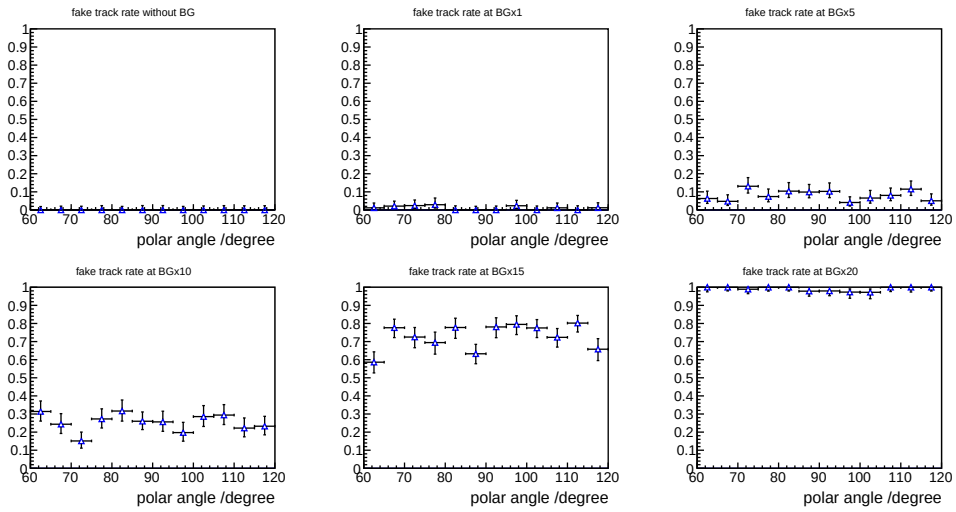

Figure 4.7: The fake track rate on each polar angle of muon at each beam background level of BGx0, BGx1, BGx5, BGx10, BGx15, and BGx20. The horizontal error bar shows the span of the bin and the vertical error bar shows the statistic error calculated by the Clopper-Pearson method.

Figure 4.7 shows the fake track rate on each polar angle of muon at each beam background level. The distribution of the fake track rates on polar angles is taken to observe the correlation between the clone track and the polar angle

of the muon, though a strong correlation is not shown. At BGx15, about 70% of the events include fake tracks. At BGx20, nearly 100% of the events include fake tracks.

4.2.4 The Effect on Fake Tracks by Using the 3D Track Trigger

Though the topic in this thesis is focused on the 2D track trigger, some studies on the 3D track trigger have to be introduced for two reasons. Firstly, the 2D track trigger only uses 5 axial super layers, while the 3D track trigger uses all 9 super layers including the other 4 stereo super layers and can measure the z of the tracks. It is reasonable for the 3D track trigger to have stronger robustness to fake tracks. It is a straightforward idea to try resolving the problem of fake tracks by the 3D track trigger. Secondly, the trigger conditions used to simulate the trigger rate caused by fake tracks require at least one 3D track as introduced in the next section. It is kind of meaningless to simulate the trigger rate without consideration of the 3D track trigger. Here we evaluate the robustness t fake tracks of the 3D track trigger by the same method introduced in Section 4.2.2.

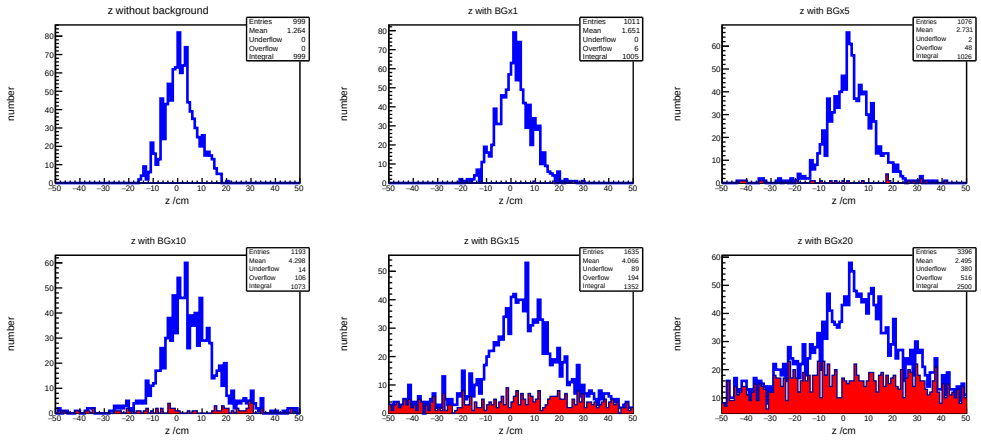

Figure 4.8: z reconstructed by the 3D track trigger at each beam background level of BGx0, BGx1, BGx5, BGx10, BGx15, and BGx20. The blue lines correspond to all reconstructed tracks and the red part corresponds to ghost tracks which are the fake tracks unrelated to the signal track.

Figure 4.8 shows the distribution of z reconstructed by the 3D track trigger. Without the beam background, the z of a part of the reconstructed signal tracks can reach near 20 cm. The width widens with the effect of the beam background. At BGx20, most of the tracks are fake tracks, and the z of them concentrate within ± 40 cm. As it is not clear about the real width of the z of the reconstructed 3D tracks at the targeted luminosity and the z of a large number of fake tracks concentrate within ± 40 cm, the effect of the z on eliminating fake tracks is limited. In this simulation, we mainly consider the effect of using the other 4 stereo super layers on eliminating fake tracks. Figure 4.9 shows the number of reconstructed

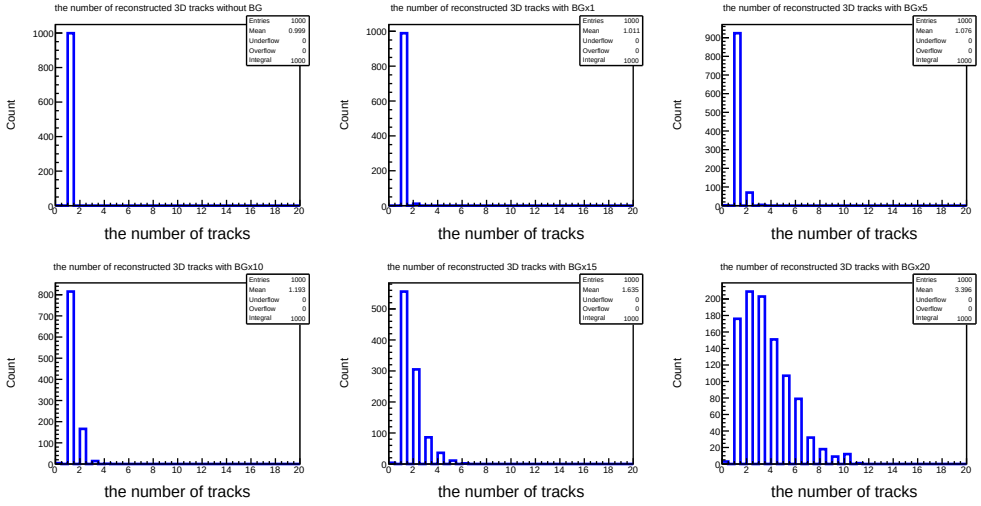

Figure 4.9: The number of reconstructed 3D tracks at each beam background level of BGx0, BGx1, BGx5, BGx10, BGx15, and BGx20.

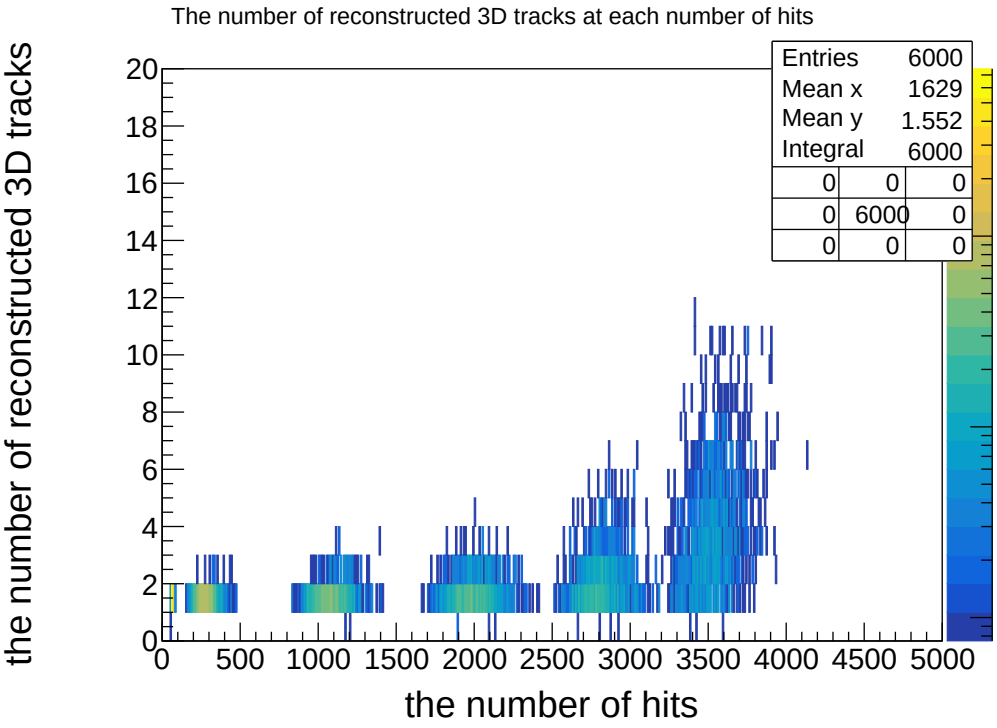

Figure 4.10: The number of reconstructed 3D tracks also increases rapidly at a high number of hits like Fig. 4.6. The number of reconstructed 3D tracks decreases to about a half compared to the number of reconstructed 2D tracks at the same number of hits.

3D tracks. More than 50% of the events do not include a fake track at BGx15 and about 18% of the events do not include fake tracks at BGx20. Both the percentage of events without fake tracks and the number of fake tracks are improved in the 3D track trigger. Fuguire 4.10 shows a similar trend that fake tracks rapidly increase at a high number of hits, while the number of fake tracks decreases to about a half by the 3D track trigger. Both the two figures show stronger robustness to fake tracks of the 3D track trigger than that of the 2D track trigger.

4.2.5 Trigger Rate Caused by Fake Tracks

To simulate the trigger rate caused by fake tracks, here we only consider two typical kinds of trigger conditions a high-background environment as shown below. If any other condition is added, the trigger rate should be even higher. The first condition is to trigger complex events such as $\Upsilon(4S) \to B\bar{B}$ and the second condition is to trigger events like dimuon.

1. More than three 2D tracks are reconstructed and at least one 3D track is reconstructed.

2. Two 2D tracks are reconstructed with an open angle larger than 90° and at least one 3D track is reconstructed.

In the simulation, we only simulate the beam background without simulating the muon. The percentage of the simulated events that pass through any one of the two trigger conditions is calculated, which shows the probability of a level-1 trigger signal to be sent within a time window of 1 μs. Therefore, the percentage is actually the trigger rate caused by fake tracks in a unit of "/μs" or "MHz".

Table 4.3: Beam-background trigger rate. The errors are statistical errors calculated by the Clopper-Pearson method.

BG level	trigger rate /kHz
BGx10	$7.0^{+3.7}_{-2.6}$
BGx15	141^{+12}_{-11}
BGx20	695^{+15}_{-15}

Table 4.3 shows the simulated trigger rate caused by the beam background. At BGx15 and BGx20, only the two conditions can make the trigger rate surpass the limit of 30 kHz. It is cautious that both the number of fake tracks and the trigger rate increase rapidly at a high beam background level. If the beam background is underestimated, a small amount of underestimation can cause a huge increasing of fake tracks, resulting in even higher trigger rates. It is of high priority to design a new algorithm to resolve the problem of fake tracks.

tis

Chapter 5

Full-Hit Algorithm

As discussed in Chapter 4, the trigger rate caused by fake tracks is simulated to be 141 kHz which is higher than the limit of 30 kHz at targeted luminosity. To improve the robustness to the beam background, an upgraded 2D tracker algorithm has been developed and is named "Full-hit algorithm". The concept of the Full-hit is explained in Section 5.1. The technical modifications from the conventional algorithm are discussed in Section 5.2. The performance evaluation of the Full-hit with the default parameters is given in Section 5.3 and that with other parameters is given in Section D.

As a convention, the conventional 2D tracker algorithm is denoted as "conventional 2D" and the Full-hit algorithm is denoted as "Full-hit 2D".

5.1 Concept of the Full-hit Algorithm

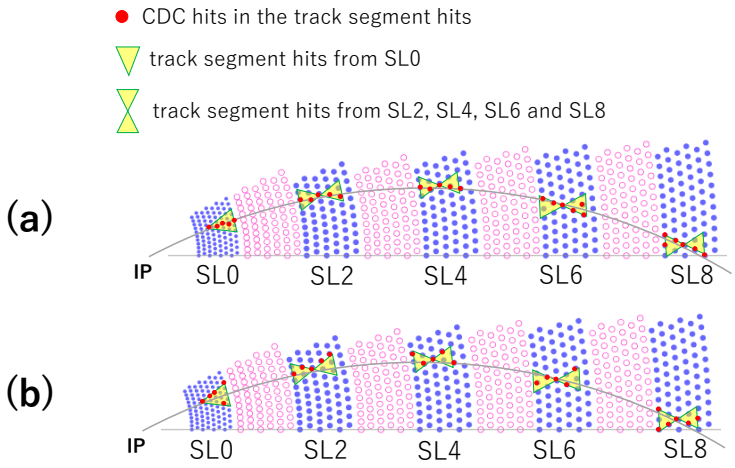

Figure 5.1: (a) an example of a reconstructed 2D track of a real charged particle. (b) an example of a fake track reconstructed by randomly distributed beam background hits.

As described in Section 3.4, only the priority hits in the track segment hits are used in the conventional 2D. As shown in Figure 5.1, both the (a) and the (b) in the figure is legal to be reconstructed by the conventional 2D as the conventional 2D does not use the hit-pattern within the track segment hits. However, the hit-patterns among the track segment hits of the real charged particle show a

consistency that the CDC hits within them are closer to the track than that of the fake track. It is difficult for fake tracks to form such consistency by randomly distributed hits. Therefore, fake tracks like (b) is expected to be eliminated by making use of the hit-patterns within the track segment hits.

Fig. 5.2 and Fig. 5.3 show the same simulated event reconstructed by the conventional 2D as shown in Fig.5.2 and the Full-hit 2D as shown in Fig.5.3, in which the Full-hit 2D uses the default setting introduced in the next section. In this event, there are three regions within the hough grid where clusters concentrate. The color in the hough grid outside the cluster of the real track shown in Fig.5.2 is lighter than that shown in Fig.5.3. That is to say, the z-value outside the cluster of the real track becomes smaller in the hough grid of the Full-hit 2D than that in the hough grid of the conventional 2D, which makes it difficult to coincidentally form clusters from the beam background hits. As a result, all the seven fake tracks reconstructed in the conventional 2D do not appear in the Full-hit 2D in this example.

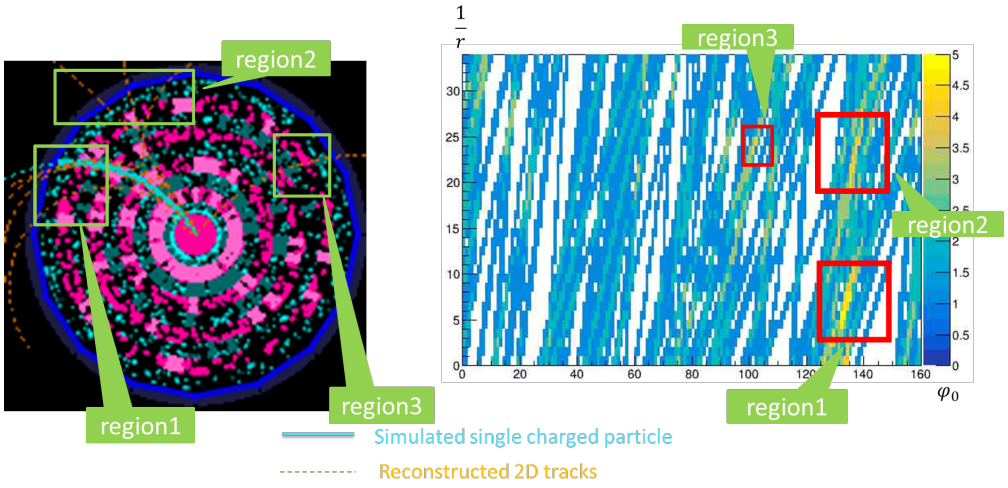

Figure 5.2: The example event reconstructed by the conventional 2D track trigger. The right plot shows the corresponding hough grid of the event shown left.

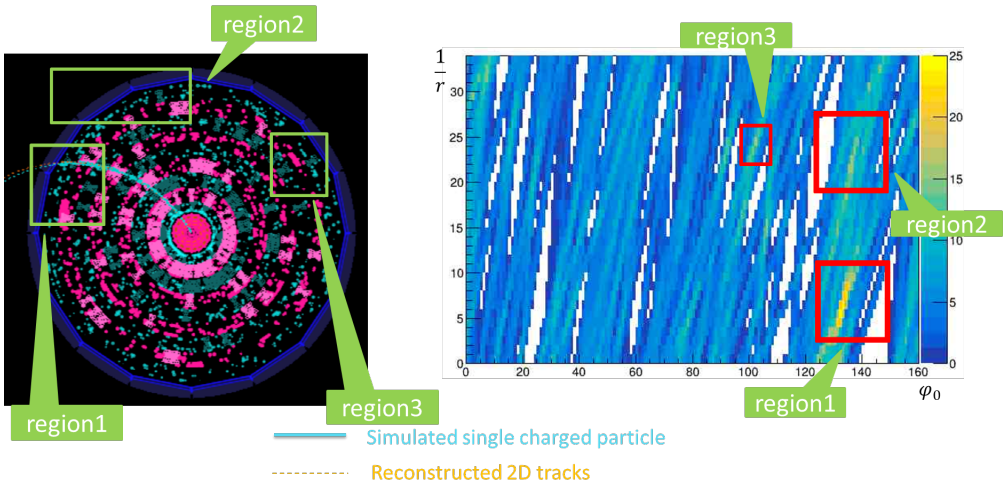

Figure 5.3: The example event reconstructed by the full-hit 2D track trigger. The right plot shows the corresponding hough grid of the event shown left.

5.2 Design of the Full-hit Algorithm

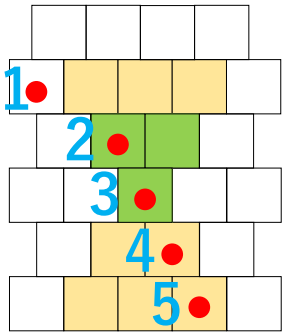

Figure 5.4: The red hits are CDC hits. The colored cells form the example track segment hit.

As the name "Full-Hit algorithm" shows, all the hits in one track segment hit, instead of priority hit only, should participate in the track reconstruction. For the example shown in Fig. 5.4, only the hit with number 3 participates in the track reconstruction in the conventional 2D. While in the Full-hit 2D, the hits with number 2,3,4,5 that are within this track segment can all participate in the track reconstruction. The hit with number 1 cannot be involved in the track reconstruction because it is not a part of the track segment hit.

In the Full-hit, all CDC hits within the track segment hits are transformed to hough curves in the parameter space of φ_0 and $1/r$ according to Eq. 5.1 which is similar to Eq. 3.2 but the position of the priority hit is substituted by the position of any hit (r_{hit}, φ_{hit}) in a track segment hit. As the number of used layers within a track segment hit increases from 2 to 5 in the Full-hit 2D, the list of r_{hit} in the algorithm has been updated as shown in Table 5.1. The φ_{hit} of the first priority cells is $n\frac{2\pi}{N_c}$ for a track segment ID 'n', which is the same as that in the conventional 2D. The φ_{hit} for other cells is the sum of the φ_{hit}s of the first priority cell and the staggered angle with respect to the first priority cell. Figure 5.5 shows the staggered angle of each cell with respect to the first priority cell with a unit of $\frac{\pi}{N_c}$ where N_c denotes the number of cells at each layer within the super layer.

$$\frac{1}{r} = \frac{2}{r_{hit}} \times \sin(\varphi_0 - \varphi_{hit}) \tag{5.1}$$

For the hough grid in the conventional 2D, it makes sense that two track segment

Table 5.1: r_{hit} at each layer of SL0, SL2, SL4, SL6, SL8. The layer number counts from the inner to the outer.

layer number in the super layer	0	1	2	3	4
SL0	19.80	20.80	21.80	22.80	23.80
SL2	36.52	38.34	40.16	41.98	43.80
SL4	58.41	60.18	62.00	63.82	65.64
SL6	80.25	82.02	83.84	85.66	87.48
SL8	102.09	103.86	105.68	107.50	109.32

hits from the same super layer are not repeatedly counted in one cell. In the Full-hit, we should take similar measures to avoid meaninglessly increasing z-value of

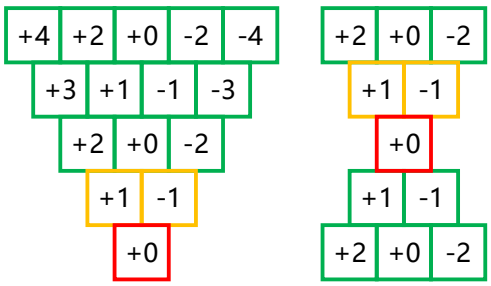

Figure 5.5: The staggered angle of each cell with respect to the first priority cell with a unit of $\frac{\pi}{N_c}$.

the cells in hough grid. As the basic units transform to CDC hits instead of track segment hits (represented by priority hit), the basic division degrades from super layer to layer. In the Full-hit 2D, we regulate that the hits from the same layer cannot be repeatedly counted in one cell. Therefore, the maximum value of z for every cell raises to 25 from 5 by this modification. Imitating the ratio of 4 to 5 for the threshold of peak candidates in the conventional 2D, we set the default value of threshold of peak candidates N_{hits} in the Full-hit is to be 20 in the Full-hit 2D. The default values of other parameters such as N_{cells} or the number of bins are the same with that in the conventional 2D.

The main differences between conventional 2D and the Full-hit 2D are summarized below:

(1) All CDC hits (only the priority hit) within track segment hits are used for track reconstruction in the Full-hit 2D (conventional 2D).

(2) The CDC hits (track segment hits) from the same layer (super layer) are not repeatedly counted in one cell in the Full-hit 2D (conventional 2D).

(3) The maximum value of z denoting the number of passing curves from different layers (super layers) in the cell is 25 (5) in the Full-hit 2D (conventional 2D).

(4) The default value of the threshold of peak candidates is 20 (4) in the Full-hit 2D (conventional 2D).

The default values of the parameters of the Full-hit 2D are listed as follows:

1. The threshold of peak candidates: N_{hits} is 20.
2. The least required number of peak candidates for every cluster N_{cells} is 2.
3. The number of bins of φ_0 $(1/r)$ of hough grid N_{φ_0} (N_w) is 160 (34).

5.3 Performance Evaluation of the Full-Hit Algorithm with Default Parameters

In this section, the performance of the Full-hit is evaluated basically with the same methods used in Section 4.2. The reconstruction efficiency, fake track rate, the number of fake tracks, and the trigger rate caused by fake tracks are evaluated and compared with the conventional 2D.

Figure 5.6, the reconstruction efficiency is kept at most range of muon polar angle, though with a drop of about 5% at around 120°, which corresponds to the back-end part of the CDC. Figure 5.7 shows that the fake track rate is about 15% at BGx15 and about 20% at BGx20. Compared with about 70% at BGx15 and about 100% at BGx20 in the conventional 2D shown in Fig. 4.7, the fake track

rate in the Full-hit has improved a lot.

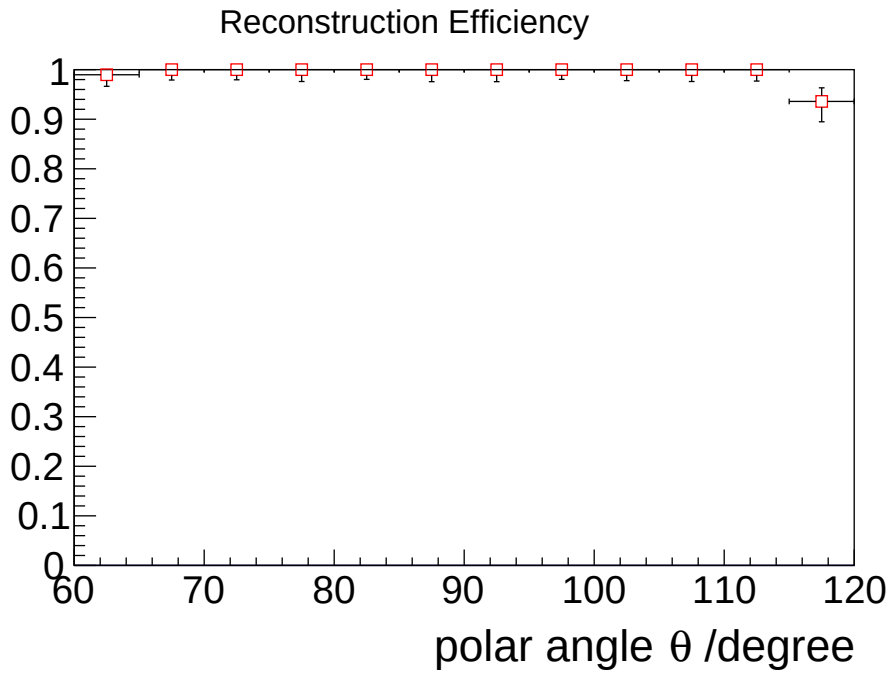

Figure 5.6: The reconstruction efficiency as a function of the muon polar angle. The horizontal error bar shows the span of the bin and the vertical error bar shows the statistic error calculated by the Clopper-Pearson method.

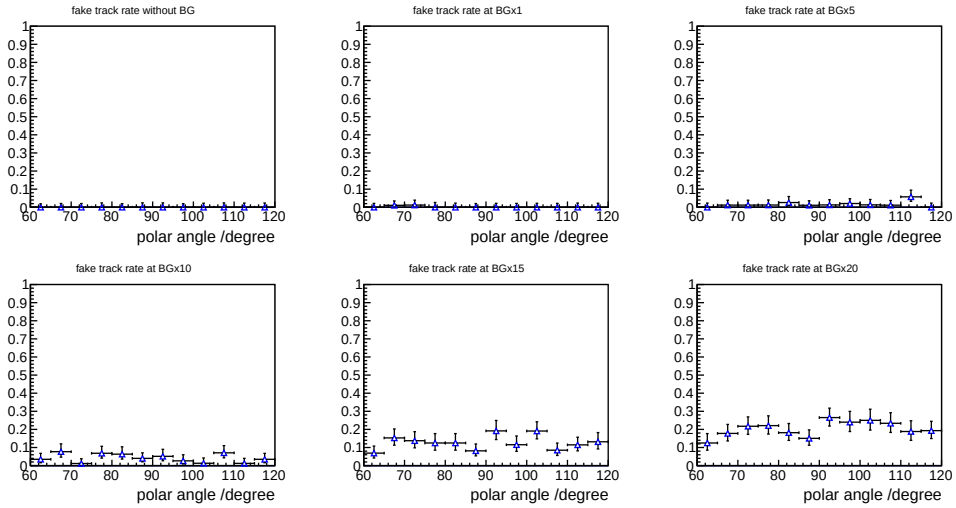

Figure 5.7: The fake track rate as a function of the muon polar angle at BGx0, BGx5, BGx10, BGx15, and BGx20. The horizontal error bar shows the span of the bin and the vertical error bar shows the statistic error calculated by the Clopper-Pearson method.

Fig. 5.8 shows the number of reconstructed 2D tracks at each number of hits in an event, in which the upper plot shows the simulated conventional 2D and the lower plot shows the Full-hit 2D. The number of fake tracks increases rapidly at a high number of hits in the conventional 2D, while the number of fake tracks majorly concentrates at 1 even with BGx20 in the Full-hit 2D, which accords with the ideal expectation.

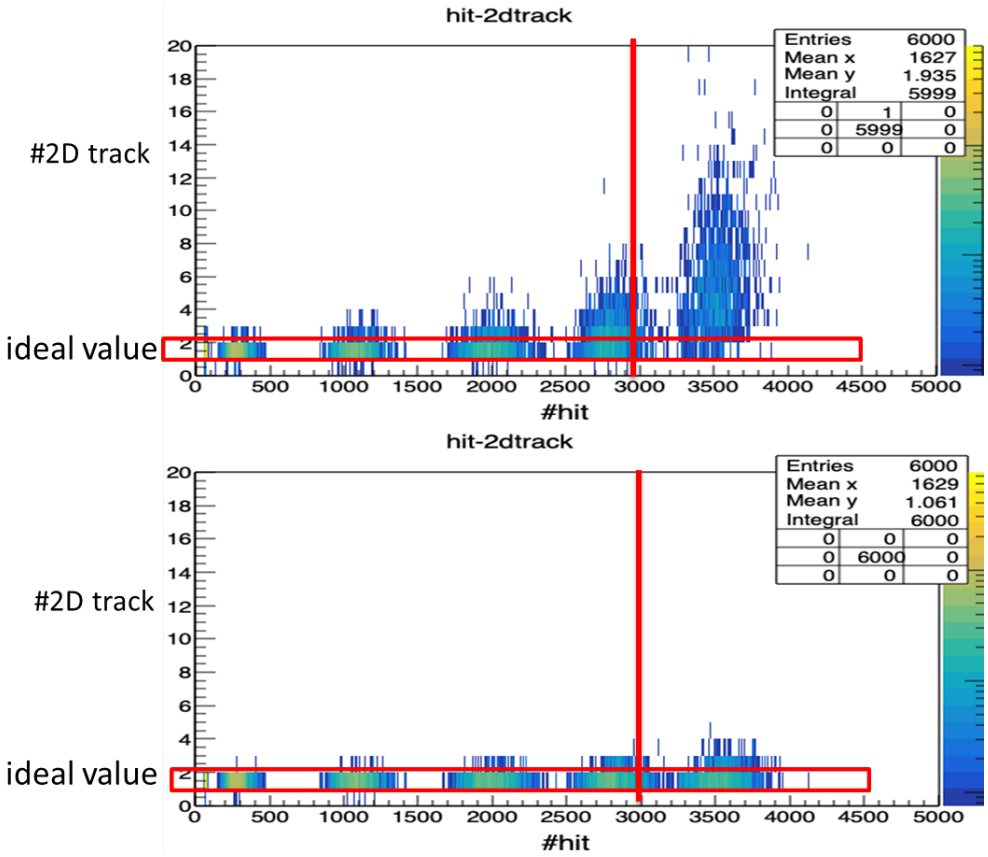

Figure 5.8: The correlation between the number of hits in a time window and the number of reconstructed 2D tracks. The upper plot shows the conventional 2D and the lower plot shows the Full-hit 2D. As there is a simulated muon, the ideal number of reconstructed 2D tracks is 1.

Table 5.2: Comparison between the trigger rates caused by fake tracks of the Full-Hit 2D and of the conventional 2D. The errors are statistical errors calculated by the Clopper-Pearson method.

BG level	trigger rate /kHz (full-hit 2D)	trigger rate (conventional 2D) /kHz
BGx10	$0.0^{+0.18}_{-0.0}$	$7.0^{+3.7}_{-2.6}$
BGx15	$0.0^{+0.18}_{-0.0}$	141^{+12}_{-11}
BGx20	$7.0^{+0.8}_{-0.9}$	695^{+15}_{-15}

Tab.5.2 shows the trigger rate caused by fake tracks estimated by the same method described in Section 4.2.5. The trigger rate caused by fake tracks at targeted luminosity is expected to be 0.0 kHz, which means that there are no triggered events within the 10,000 simulated events.

However, the BGx20, which is higher than the expected beam background level at the targeted luminosity BGx15, does not show a totally acceptable trigger rate of 7.0 kHz, which reaches about 1/4 of the limit of 30 kHz. If BGx15 is an underestimated beam background level at the targeted luminosity, the Full-hit 2D with default parameters cannot ensure the smooth operation of the 2D track trigger. Therefore, an attempt of parameter tuning has also been conducted and some sets of parameters have been found able to suppress the trigger rate caused by fake tracks below 2 kHz at BGx20. The details are elaborated in Appendix D.

5.4 Summary

The development of the Full-hit Algorithm and the great improvement in the robustness to the beam background shown by the Monte Carlo simulation are the main achievements in this study. By using the Full-hit 2D with default parameters, the fake track rate decreases to 15%, and the trigger rate caused by fake tracks decrease to 0.0% at the targeted luminosity. Moreover, a backup solution of parameter tuning has also been prepared in case the beam background level at the targeted luminosity is underestimated.

Chapter 6

Development of Full-Hit Algorithm on FPGA Firmware

The technical modifications on the FPGA firmware to realize the Full-hit 2D in Section 6.1. Some preliminary achievements in the commissioning is given in Section 6.2. The remaining works of the commissioning are listed in Section 6.3.

6.1 Modifications on the Firmware of Full-Hit Algorithm

The Full-hit 2D firmware cannot be implemented without the upgrading of the trigger universal board from UT3 to UT4. In the UT3, the bandwidth in a clock from the TSF modules to the 2D tracker modules was 340 bits, in which 324 bits have been used. The remaining space is not enough for transferring the hit-patterns of the track segment hits that need 15 bits for each one of the 15 track segment hits. Moreover, the resource usage of the look-up table (LUT) reaches over 90% for the Full-hit 2D firmware on the UT4 with VU80 introduced in Section 3.2. Such usage of the LUT cannot be provided by a UT3 board. The transferring of the hit-patterns is discussed in Section 6.1.1 and the modifications of each sub-modules are discussed in Section 6.1.2.

6.1.1 Modification of the Data Transmission from TSF Modules to the 2D tracker modules

The conventional configuration of the transmission from TSF modules to a 2D tracker module does not include the inner hit-patterns of the track segment hits, which is necessary for the Full-hit 2D firmware. To import the information of hit-patterns, the spare space created by the upgrading to UT4 has been used as shown in Fig. 6.2 where the TSF0, TSF2, TSF4, TSF6, and TSF8 are the TSF modules that find track segment hits within axial super layers respectively of SL0, SL2, SL4, SL6, SL8. To keep the consistency with the conventional 2D firmware, the locations of originally used space were not changed. Every track segment hit in TSF0 has 15 CDC cells, while every track segment hit in TSF2, 4, 6, 8 has 11 CDC cells. To save as much space as possible, the bitmap from TSF0 to 2D module and the bitmap from TS2, 4, 6, 8 to a 2D module have been separated into two patterns instead of providing 15 bits for each hit-pattern for all track segment hits.

6.1.2 Modifications of each sub-module

The original functions of each sub-module in the conventional 2D have been introduced in Section 3.4.2. Figure 6.3 shows the schematic diagram of the data

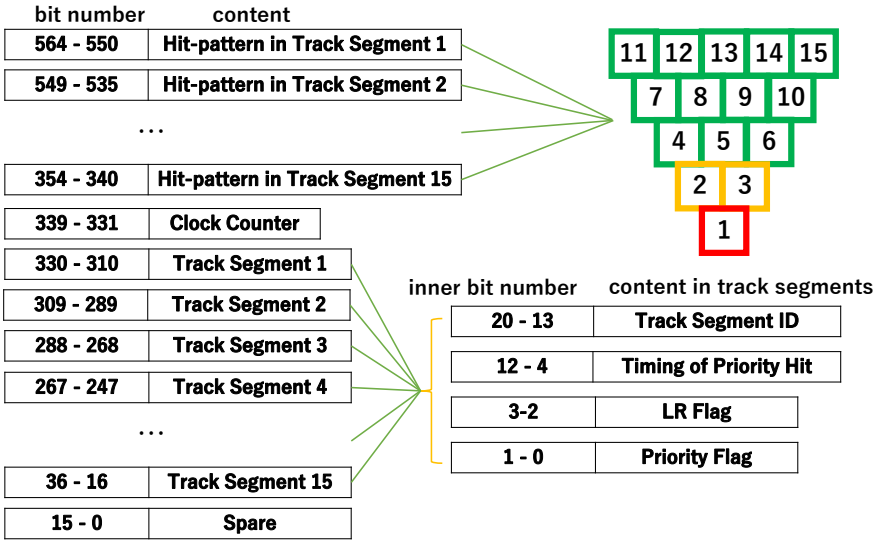

Figure 6.1: Bitmap from the TSF0 module to the 2D tracker module.

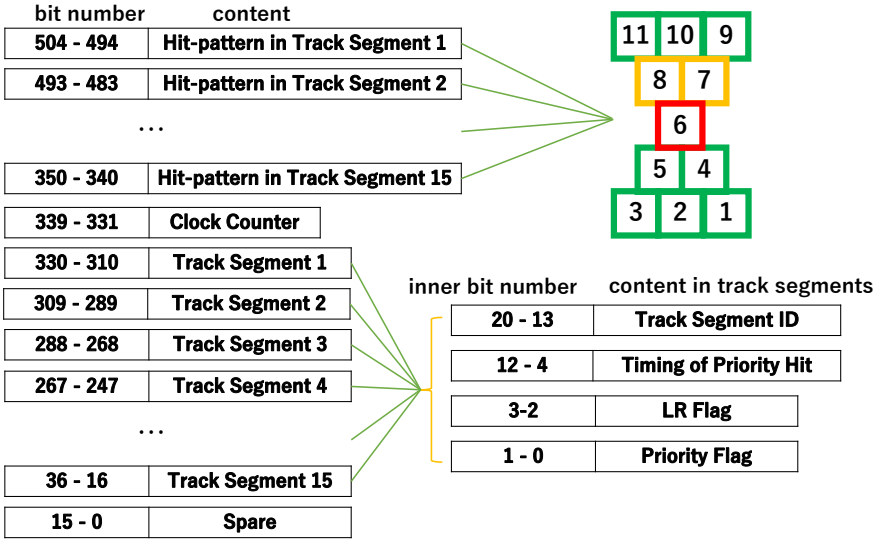

Figure 6.2: Bitmap from the TSF2, TSF4, TSF6 and TSF8 modules to the 2D tracker module.

flow in the Full-hit 2D firmware with the modified sub-modules reddened. With the modification of the bitmap from the TSF modules to the 2D modules, the Full-hit 2D firmware deals with the added optical receivers that transfer hit-patterns of the track segment hits. To keep the consistency with the conventional 2D firmware, the information of hit-patterns is processed independently of the original parts but within the same clock domain. To provide convenience for commissioning, the function of adjusting the threshold of peak candidates N_{hits} from VME has been added. The transmission between the registers of the N_{hits} and the VME has been added to the top module.

In the persistor module, the transferring of the hit-maps with positions of priority hits has been expanded to the hit-maps with hit-patterns. As introduced in Section 3.4.2 and Section 6.1, the CDC hits (track segment hits) from the same layer (super layer) are not repeatedly counted in one cell in the Full-hit

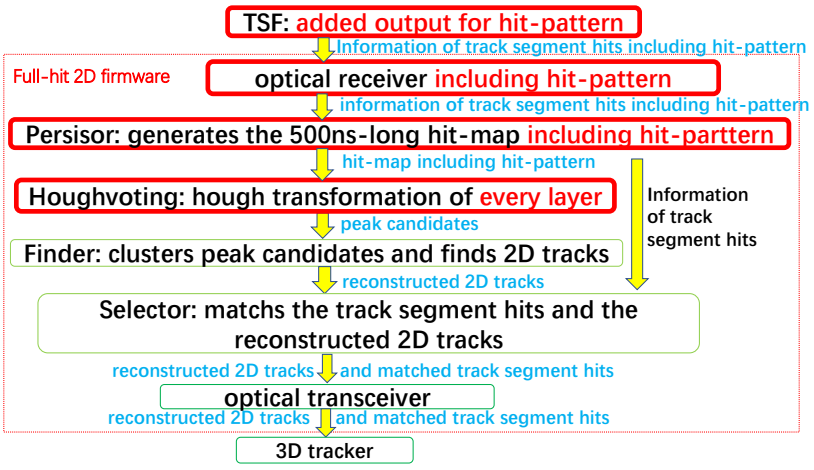

Figure 6.3: The schematic diagram of the data flow in the Full-hit 2D firmware. The red sub-modules are modified.

2D (conventional 2D). The conventional 2D firmware does the parallel hough transformation of each axial super layer and merges the 5 hough grids from the 5 axial super layers into one hough grid with judging the peak candidates at the same time. The Full-hit 2D firmware imitates the same method. The Full-hit 2D firmware does the parallel hough transformation of each used layer in the 2D track trigger and merges the 25 hough grids of the 25 layers into one hough grid with judging the peak candidates at the same time. As a result, the number of parallel mapping raises from 5 to 25. There are at least 11 CDC cells in every one of the 2336 track segments and there are 160×34 cells in hough plane. The high complexity of the mapping from hit-maps to hough grids uses a large proportion of logic resources in FPGA at least 5 times higher than that of the conventional 2D tracker firmware. The huge scripts that write down all mapping relations from hit-map to hough plane are automatically generated based on Eq. 5.1.

The mathematical logic of judging peak candidates is similar to that in the conventional 2D. To determine whether a cell in the hough grid is a peak candidate, the number of "1" at the cell of all 25 hough grids is counted. The cell is a peak candidate if the number of "1" is higher than the threshold. As the threshold in the Full-hit 2D is adjustable, a function has been added to the Houghvoting module to count the number of "1" and judge whether the number satisfies the threshold.

6.2 Commissioning of the Full-hit 2D Firmware

The Full-hit 2D firmware has been successfully implemented. The resource usage of the Full-hit 2D firmware, the setting up of the commissioning, the confirmation with eye level by the Integrated Logic Analyzer (ILA), and the Belle II link are discussed in this section.

6.2.1 Resource Usage

we have installed the Full-hit 2D onto a VU160 board whose specifications are shown in Section 3.2. The implementation was successful in satisfying the timing

Table 6.1: Resource usage of the Full-hit 2D firmware on a VU160 board

Resources of Full-hit 2D on VU 160	Usage
Look-up table (LUT)	45%
RAM for LUT	9%
Flip-flop registers (FF)	5%
Block RAM (BRAM)	3%
IO	21%
Gigabit transceiver (GT)	32%
Global buffer (BUFG)	3%
Mixed-mode clock manager (MMCM)	11%

requirement and the limited resources. As shown in Table 6.2.1, the usage of the look-up tables (LUT) is 45%, which is about a half higher than the conventional 2D firmware. The increase of the LUT usage is thought to be caused by the higher complexity of the mapping in the hough transformation as described in Section 6.1.2.

6.2.2 Setting Up

We have installed the VU160 board with FUll-hit 2D firmware into the real Level-1 Trigger system in operation as shown in Fig. 6.4, in order to take real-time collision data. To avoid disadvantages to the operation, the board is installed independently with the board in operation for physics data, while sharing part of the same input from the TSF modules. CDC hits with φ_{hit} from 45° to 135° are received. The data can be read out by the Belle II link to be analyzed offline.

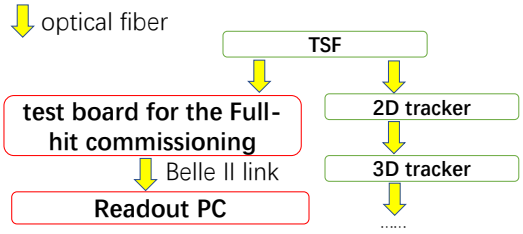

Figure 6.4: The VU160 board with Full-hit 2D firmware has been installed independently of the 2D tracker modules in operation. The output data is read out by the Belle II link.

6.2.3 Preliminary Confirmation at Eye Level

We have confirmed the data flow related to the modified sub-modules shown in Fig. 6.3 by the Integrated Logic Analyzer (ILA) with eye level. For example, we

checked the persistor module by confirming whether the corresponding register at a hit-map of a track segment hit becomes '1'. As the explanation of the confirmation is lengthy and not helpful for understanding, the contents are expanded in Appendix C.

From the readout data by the Belle II link, we can directly see the reconstructed 2D tracks by the Full-hit 2D firmware and qualitatively evaluate the performance. Figure 6.5 shows an example of a successful reconstructed 2D track by the Full-hit 2D firmware. The quantitative evaluation is in progress.

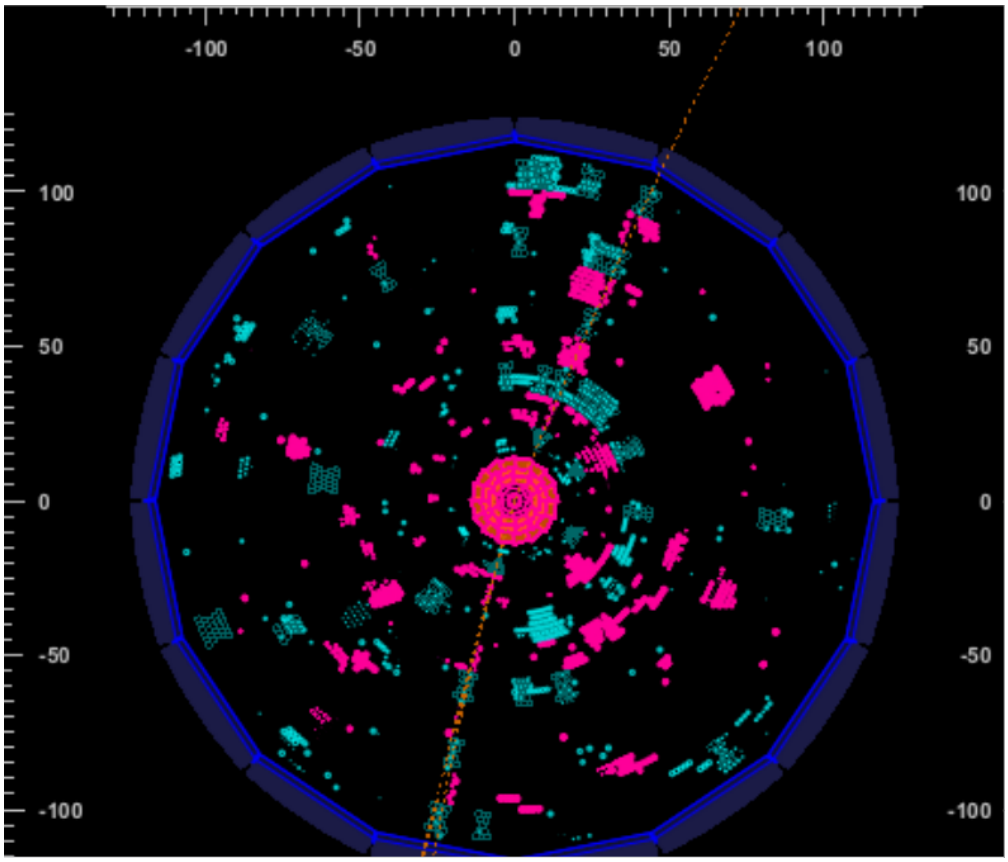

Figure 6.5: The upper orange track is reconstructed by the VU160 board with Full-hit 2D firmware, which only receives the hits with φ_{hit} from 45° to 135°. The lower orange track is reconstructed by the conventional 2D.

6.3 Remaining Works of the Commissioning

The commissioning is still in progress. The plan for the commissioning in future is listed below:

- We will compare the reconstructed 2D tracks by the Full-hit firmware and the reconstructed 2D tracks by the Full-hit simulation software with the same input of CDC hits to confirm that the Full-hit firmware is correctly designed as expected.
- We will use collision data to evaluate the reconstruction efficiency of the Full-hit firmware by comparison with the reconstructed tracks by the offline full tracking simulation.

- We will use collision data to evaluate the robustness of the Full-hit firmware to the beam background by increasing the noise hits of the CDC with a low threshold for CDC hits.
- We will design a Full-hit 2D firmware with optimized parameters shown in Appendix D.
- We will try to optimize the resource usage of the Full-hit 2D firmware.

Chapter 7

Conclusions

The Belle II experiment, an intensity frontier experiment, is aimed to measure weak interaction parameters more precisely and find new physics beyond the Standard Model such as dark sector physics. The designed luminosity of the Belle II is $6 \times 10^{35}\,\mathrm{cm}^{-2}\mathrm{s}^{-1}$, which is 30 times higher than the predecessor.

Accompanied by the unprecedentedly high luminosity is a beam background that is several tens of times higher than the predecessor. A Monte Carlo simulation of the targeted luminosity has been conducted to evaluate the performance of the 2D track trigger in the face of the high beam background. At the simulated targeted luminosity, more than half of the events have at least one fake track reconstructed by the beam background hits, and the trigger rate caused by the fake tracks is expected to be 141 kHz, which is higher than the limit of 30 kHz. Obvious improvements have not been observed by adjusting the parameters of the 2D track trigger as shown in Appendix B.

The Full-hit algorithm has been developed to suppress the fake tracks. The Full-hit was first implemented as a simulation software. The simulation shows that the Full-hit can suppress the fake track rate to about 15% and make the trigger rate caused by fake tracks at the targeted luminosity decrease from 141 kHz to 0.0 kHz at the targeted luminosity with keeping the damage on the reconstruction efficiency smaller than 1%. Moreover, the Full-hit with the other parameters listed in Appendix D can realize higher robustness to the beam background, considered as a backup solution when the real beam background is higher than anticipated.

The performance evaluation of the 2D track trigger, the development of the Full-hit as a simulation software, and the performance evaluation of the Full-hit are the main achievements in this study. In addition, the FPGA firmware of the Full-hit has been successfully implemented thanks to the upgrade of the Universal Trigger Board (UT) from UT3 to UT4. The setting up and the confirmation of the data flows have been conducted. The Full-hit firmware is under commissioning with the next plans listed in Section 6.3 and is expected to be put into operation in 2023 after the long shutdown of the Belle II experiment.

Bibliography

[1] Tetsuo Abe et al. "Belle II technical design report". In: *arXiv preprint arXiv:1011.0352* (2010).

[2] Belle Collaboration. "Technical design report". In: *KEK report* 95.1 (1995).

[3] Makoto Kobayashi and Toshihide Maskawa. "CP-violation in the renormalizable theory of weak interaction". In: *Progress of theoretical physics* 49.2 (1973), pp. 652–657.

[4] Emi Kou et al. "The Belle II physics book". In: *Progress of Theoretical and Experimental Physics* 2019.12 (2019).

[5] Kazunori Akai, Kazuro Furukawa, Haruyo Koiso, et al. "SuperKEKB collider". In: *Nuclear Instruments and Methods in Physics Research Section A: Accelerators, Spectrometers, Detectors and Associated Equipment* 907 (2018), p. 2.

[6] Yukiyoshi Ohnishi, Tetsuo Abe, Toshikazu Adachi, et al. "Accelerator design at SuperKEKB". In: *Progress of Theoretical and Experimental Physics* 3 (2013).

[7] H Koiso et al. "Design of SuperKEKB based on the Nano-beam Scheme". In: *KEK report* (2010).

[8] Hikaru Tanigawa. *A study of beam background from SuperKEKB on Belle II Silicon Vertex Detector*. 2019.

[9] A. Paladino. "Beam background evaluation at SuperKEKB and Belle II". In: *Journal of Instrumentation* 15.07 (July 2020), p. 7. DOI: 10.1088/1748-0221/15/07/c07023. URL: https://doi.org/10.1088/1748-0221/15/07/c07023.

[10] https://software.belle2.org/development/sphinx/online_book/fundamentals/02-datataking.html.

[11] J.Baudot et al. "Upgrade of the vertex detector of the Belle II experiment". 2020.

[12] Deepanwita Dutta et al. "Belle II silicon vertex detector". In: *Journal of Instrumentation* 12.02 (2017).

[13] http://www.jahep.org/hepnews/2014/14-2-6-BelleIIECL.pdf.

[14] R Itoh et al. "Data flow and high level trigger of Belle II DAQ system". In: *IEEE Transactions on Nuclear Science* 60.5 (2013), pp. 3720–3724.

[15] N Taniguchi. "Central drift chamber for Belle-II". In: *Journal of Instrumentation* 12.06 (2017), p. 3.

[16] Katsuro Nakamura. "Shield modification in IR". In: *37th B2GM*. 2020.

[17] Sun-Young Ryu. "CDC Beam Background". In: *38th B2GM*. 2021.

[18] Yoshihito Iwasaki, Unno, and Nakazawa. “Belle II 実験トリガーシステム”. 2015.

[19] https://belle2.cc.kek.jp/~twiki/pub/Detector/Trigger/JingGeSlides/data_bit_map.pdf.

[20] Sara Pohl and Christian Kiesling. “Track Reconstruction at the First Level Trigger of the Belle II Experiment”. PhD thesis. Munich, Ludwig-Maximilians-Universität, 2018.

Acknowledgements

Words cannot express my gratitude to Professor Yutaka Ushiroda and Dr. Taichiro Koga for their invaluable patience and guidance. This study would not have been possible without them. They taught me not only academic knowledge but also invaluable life principles. Also, I would also like to show respect for my defense committee, Professor Ishino and Professor Tanaka who patiently read this thesis and kindly pointed out the mistakes and the space for improvement. Additionally, I could not finish this study without the kind financial support from The University of Tokyo, KEK, and the Japan Student Services Organization (JASSO). I am also grateful to all researchers and other students in the Ushiroda Lab, especially to Dr. Katsuro Nakamura, Dr. Nanae Taniguchi, Dr. Yu Nakazawa, Dr. Takuto Kunigo, Dr. Hara Koji, Dr. Toru Tsuboyama, Zihan Wang, Hikaru Tanigawa, Yuma Uematsu, and Xiaodong Shi. They have been kindly helping me and solving my puzzles during this journey. Thanks should also go to the secretaries who always provide immediate backups. Lastly, I would be remiss in not mentioning my parents and my friend Manman Wei. Their belief in me has kept my spirits and motivation high during this process.

Appendix A

Loss of Reconstruction Efficiency at Back-ends out of the Magnetic Field

For the track of a negatively charged particle with initial polar angle θ and initial azimuthal angle φ_0, initial velocity v and corresponding radius $r = m_e v/B$ in the x-y plane, the curve is represented in polar coordinate as Equation A.1.

$$\begin{cases} \rho = 2r\sin(\dfrac{B}{m_e}\cdot t) \\ \varphi = \dfrac{B}{m_e}\cdot t + \varphi_0 \\ z = v\cos\theta\cdot t = \dfrac{Br\cos\theta}{m_e}\cdot t \end{cases} \tag{A.1}$$

We can get the slope factor of the track at the z-y plane and further the change of the slope factor.

$$\begin{aligned} \frac{dy}{dz} &= \frac{d(\rho\sin\theta\sin\varphi)}{dz} \\ &= \frac{d((2r\sin(\frac{B}{m_e}\cdot t)\sin\theta\sin(\frac{B}{m_e}\cdot t+\varphi_0))}{d(\frac{Br\cos\theta}{m_e}\cdot t)} \\ &= \frac{2m_e\sin\theta}{B\cos\theta}\cdot\frac{d((\sin(\frac{B}{m_e}\cdot t)\sin(\frac{B}{m_e}\cdot t+\varphi_0))}{dt} \\ &= \frac{2\sin\theta}{\cos\theta}\sin(2\frac{B}{m_e}\cdot t+\varphi_0) \\ \frac{d^2y}{dz^2} &= \frac{4\sin\theta}{r\cos^2\theta}\cos(2\frac{B}{m_e}\cdot t+\varphi_0) \end{aligned} \tag{A.2}$$

The sign of $\frac{d^2y}{dz^2}$ when $t = 0$ depends on φ_0, the initial azimuthal angle. Obviously, $\frac{d^2y}{dz^2}$ should always be 0 if without a magnetic field. If φ_0 is in the 1^{st} quadrant or 3^{rd} quadrant, the negative particle flies farther from the z-axis by the exertion of the magnetic field. If φ_0 is in the 2^{nd} quadrant and 4^{th} quadrant, the negative particle flies closer to the z-axis by the exertion of the magnetic field. The polar angle of the former kind of particle tends to increase, while that of the latter kind of particle tends to decrease. This phenomenon also contributes to the loss of efficiency at the two sides of the coverage.

Appendix B

Performance Evaluation of the 2D Track Trigger with Non-default Parameters

The default values of the parameters in the 2D track trigger were optimized by considering of the balance between reconstruction efficiency and fake tracks in an environment with low beam background. We attempted to modify the adjustable parameters to achieve higher robustness to the beam background.

There are three main controllable parameters shown as follows. w denotes $1/r$. φ_0 and r were introduced in Section 3.4.1.

1. The threshold of peak candidates N_{hits} with a default value of 20.
2. The least required number of peak candidates for every cluster N_{cells} with a default value of 2.
3. The number of bins of φ_0 $(1/r)$ of hough grid N_{φ_0} (N_w) with a default value of 160 (34).

B.1 Parameter Tuning of N_{hits}

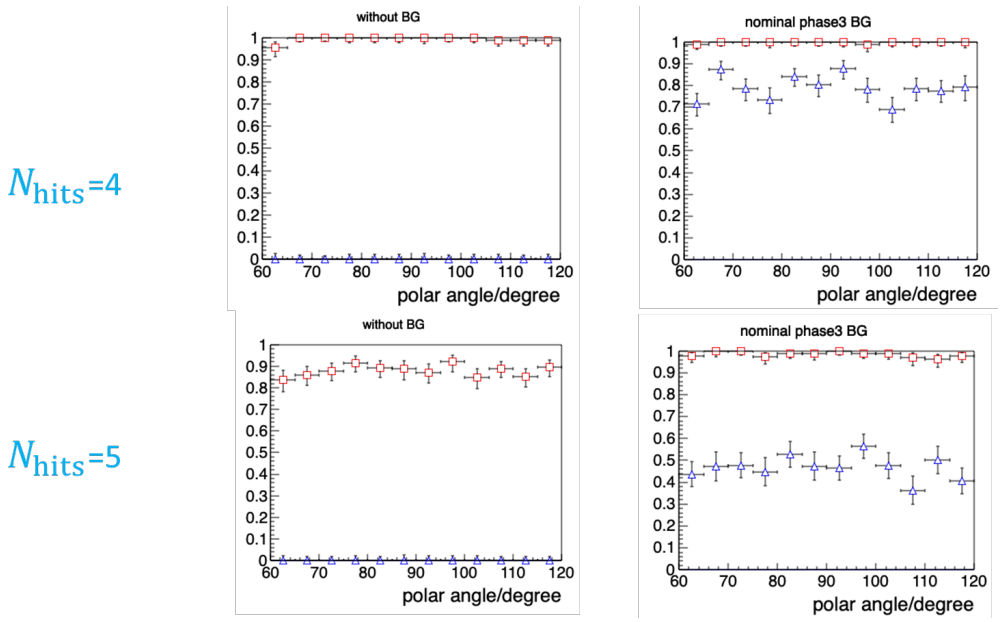

Figure B.1: The comparison between the peak candidate threshold of 4 which is the default value and 5. Red squares show the percentage of events in which the number of tracks is more than 0, which in the left two plots represent the reconstruction efficiencies at each polar angle of the simulated muon. Blue triangles show the fake track rate.

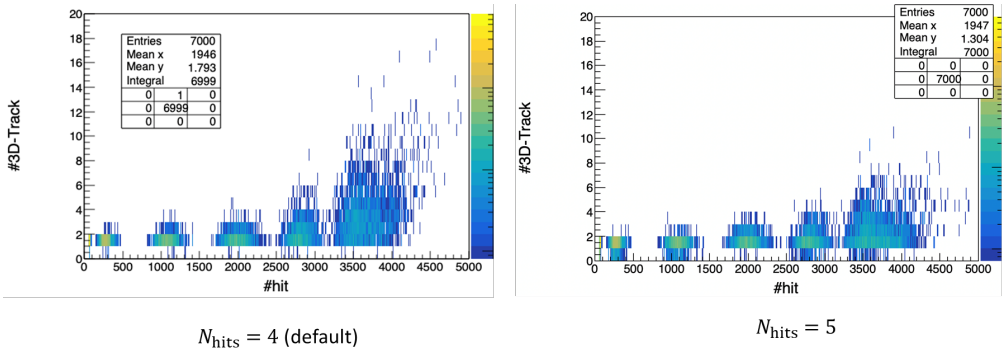

$N_{\text{hits}} = 4$ (default) $N_{\text{hits}} = 5$

Figure B.2: The number of reconstructed 3D tracks decreases to about one-half at the same beam background level.

By increasing the threshold of peak candidate N_{hits} to 5, the fake track rate decreased to about 50% with a compensation of about 10% loss of reconstruction efficiency. As only 5 axial super layers are utilized in the 2D track trigger, the maximum value 5 of N_{hit} does not forgive loss on any super layer, which is a quite strict threshold. There are several disadvantages of this measure. It is difficult for the low-momentum particles to establish track segment hits at the outermost super layer (SL8). Any one loss of the track segments excludes the possibility of the successful reconstruction if N_{hits} is raised to 5.

Though significant improvement in the robustness to the beam background has been shown in Fig. B.1 and Fig. B.2, raising N_{hit} to 5 should be a cautious decision in consideration of efficiency loss.

B.2 Parameter Tuning of N_{cells}

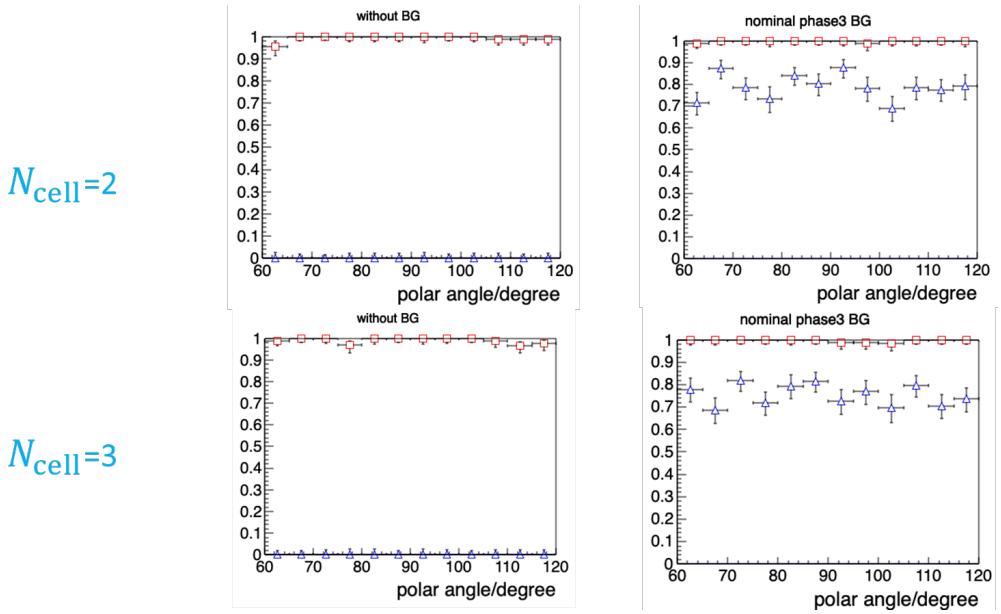

Figure B.3: The N_{cells} in the upper plot is 2 which is the default value. The N_{cells} in the lower plot is increased to 3. Red squares show the percentage of events in which the number of tracks is more than 0, which in the left two plots represent the reconstruction efficiencies at each polar angle of the simulated muon. Blue triangles show the fake track rate.

Increasing N_cell from 2 to 3 does not have significant suppression on fake tracks. The previous study in the Belle II Collaboration shows that increasing N_cell over 4 will narrow the acceptable momentum range, so the N_cell over 4 is not considered.

B.3 Parameter Tuning of N_{φ_0} and N_w

$(N_\varphi, N_R) = (160,34)$

$(N_\varphi, N_R) = (320,68)$

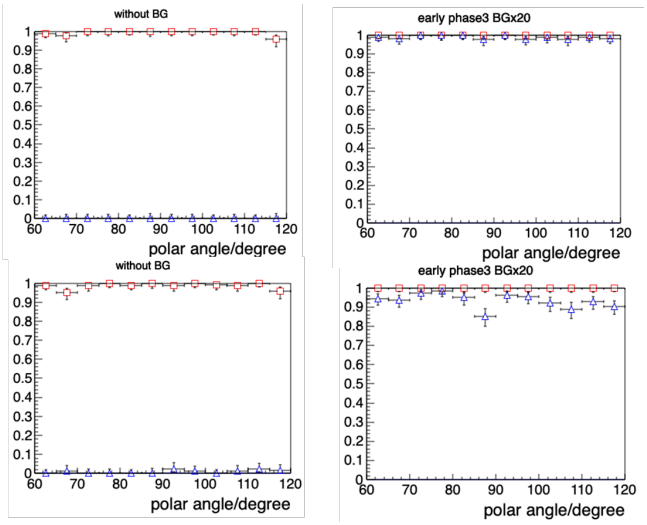

Figure B.4: The number of bins of N_{φ_0} (N_w) is 160 (34) for the upper two plots, which are the default values. The number of bins of N_{φ_0} (N_w) is 320 (68) for the lower two plots. Red squares show the percentage of events in which the number of tracks is more than 0, which in the left two plots represent the reconstruction efficiencies at each polar angle of the simulated muon. Blue triangles show the fake track rate.

$(N_\varphi, N_R) = (480,104)$

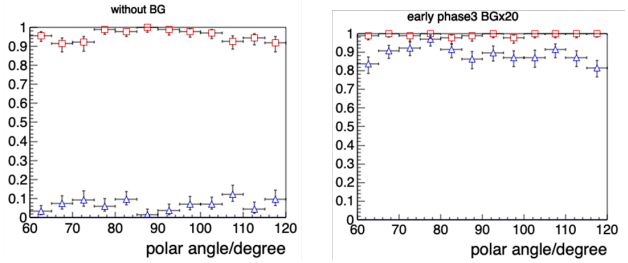

Figure B.5: The number of bins of N_{φ_0} (N_w) is 480 (104). Red squares show the percentage of events in which the number of tracks is more than 0, which in the left two plots represent the reconstruction efficiencies at each polar angle of the simulated muon. Blue triangles show the fake track rate.

The performance of the 2D track trigger is not simply positively and negatively correlated with the number of bins. If N_{φ_0} and N_w are set to be too high, one cluster might well be separated into several clusters, which is called "clone track". Also, reconstruction efficiency might decrease for higher difficulty for cells to meet the threshold of peak candidate. However, if N_{φ_0} and N_w are set to be too low, more unrelated cells can reach the threshold of peak candidate and form clusters, which is called "ghost track". Both of clone tracks and ghost tracks are fake tracks that are redundantly or falsely reconstructed.

The ratio of N_{φ_0} to N_w is optimized at $22 - 26$ by a previous study in the Belle II Collaboration. Therefore, the adjusted N_{φ_0} to N_w increases or decreases with the same factor.

As one of the examples, Fig. B.4 shows that doubling N_{φ_0} and N_w does not show significant improvement in the robustness to the beam background. Modifications of N_{φ_0} and N_w cannot help much on beam background robustness. Figure B.5 shows that 3-fold N_{φ_0} and N_w can cause obvious efficiency loss without getting satisfactory suppression of fake tracks.

Appendix C

Confirmation of Data Flow by Integrated Logic Analyzer

The first commissioning was to confirm the consistencies among the data of each sub-modules by the tool Integrated Logic Analyzer (ILA). It is a tool to observe the status of the inner registers directly at the GUI of Vivado, by which the following consistencies in each sub-modules have been confirmed.

1) The transmission of the hit-patterns of each track segment hit has been confirmed.

2) The hit-map of every layer is correctly generated based on the data of track segment IDs.

3) The mapping of hough transformation among the priority hits in the Full-hit 2D firmware is the same as that in the conventional 2D tracker firmware.

4) The consistency between the clock position of every newly added register and that of the original registers expected to work in the same domain has been confirmed.

5) The reconstructed peak candidates satisfy the preset threshold N_{hits}.

Figure C.1 shows the registers of sub-modules that are observed in the ILA, based on which the procedures of the confirmations e are to be expanded below.

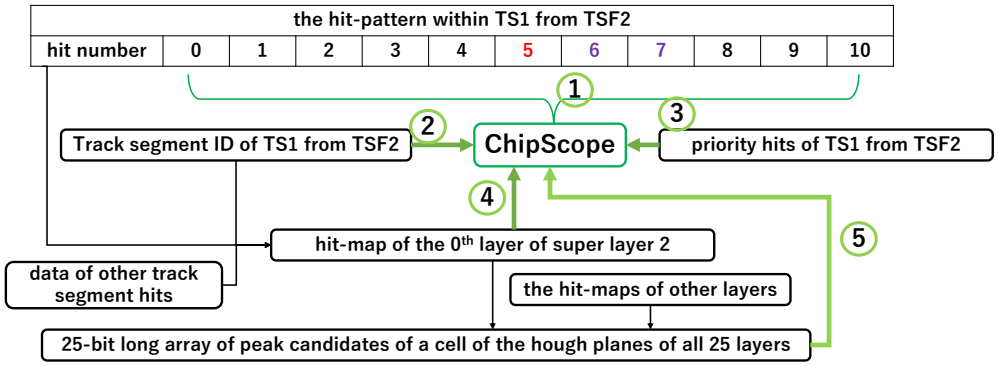

Figure C.1: the registers of sub-modules that are observed in the ILA and the data flow

C.1 Confirmation of the Hit-patterns

In the hit-pattern within TS1 from TSF2, two kinds of consistencies are confirmed:

1) The hit-patterns (① in Fig C.1) satisfy the condition of a track segment to be deemed as a track segment hit (4 layers out of 5 layers have CDC hits).

2) The hits of the priority cells (priority hits) in the hit-pattern are the same between hit-patterns and the registers of priority hits that originally exists in the conventional 2D firmware (③ in Fig C.1)).

Figure C.2: The upper row is the 11-bit hit-pattern and the lower row is the priority flag (100: first priority cell, 010: second left priority cell, 001: second right priority cell). The marked number "011" is the part of priority cells.

Figure C.2 which is a screenshot of Vivado (Virginia Design Suite, the EDA for designing Xilinx FPGAs) shows an example of the above confirmation. For the hit-pattern of "000001101111001", the left 4 '0's are redundant, and it shows that the hit-maps within the track segment on the fifth layer is '011', on the fourth layer is '01', on the third layer is '1', on the second layer, is '11' and on the first layer is '001' (all from left to right). It satisfies the condition of a track segment hit. Moreover, the priority hit accords with the priority flag that the priority it should be the first priority cell. Such comparisons were repeated to confirm that the information of hit-pattern of each track segment hit is correctly received from TSF modules.

As the priority flag is the register originally existing in the conventional 2D firmware, this comparison also verifies that these newly added registers of hit-patterns work in the expected clock domain.

C.2 Confirmation of the Generated Hit-maps

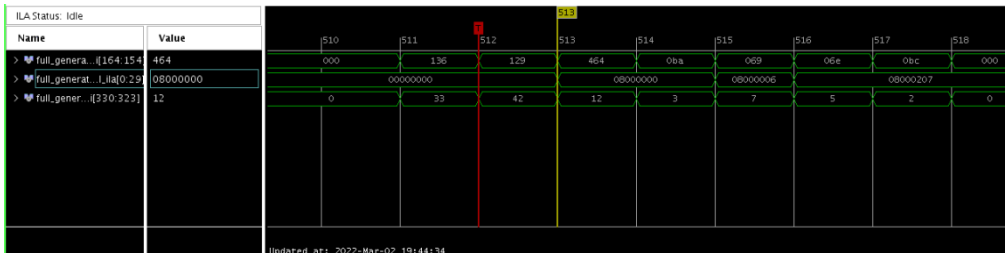

Figure C.3: The first row is the hexadecimal expression of the hit-pattern of TS1 from the TSF2 module (① in Fig. C.1), and the second row is the hexadecimal expression the hit-maps of the 41st to the 70th cells of the first layer of SL2 (④ in Fig. C.1) and the third row is the track segment ID of TS1 from the TSF2 module (② in Fig. C.1). The hit-map is one clock later than the other two registers.

Figure C.3 which is also a screenshot of Vivado shows an example of the confirmation of generated hit-maps by the "persistor" module. Only the hit-maps of the 41st to the 70th cells of the first layer of SL2 are concerned in this example. At the triggered time domain (the 512th clock), the hit-pattern of TS1 from the TSF2 module was '00100101100' by binary form, which shows that the

hit-maps within the track segment on the first layer are '100' (from left to right). As the bit number of the hit-map is anti-clockwise (from right to left) and the track segment ID is 42, the 43rd cell of the first layer of SL2 should be a CDC hit. As there are 2 redundant '0's at left, the hit-map should be '00001xxxxx...' (x means arbitrary), which accords with the observed hit-map. Such comparisons were repeated to confirm the correctness of the generated hit-maps of every layer.

C.3 Confirmation of the Found Peak Candidates

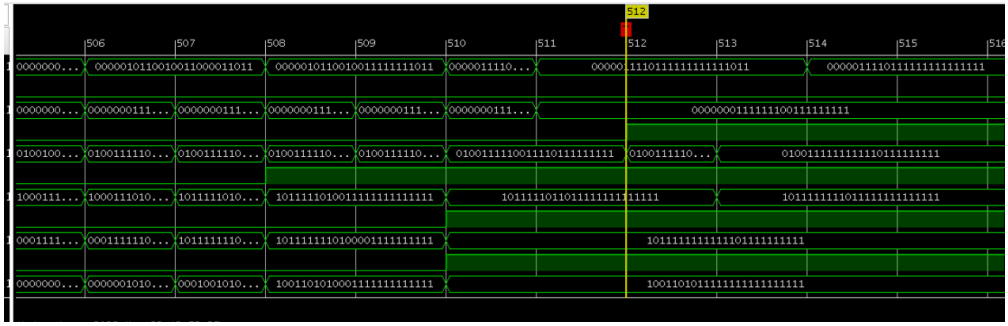

Figure C.4: The rows with numbers show the 25-bit array of peak candidates of the selected cell in the hough planes of all 25 layers (⑤ in Fig. C.1). The corresponding wave over the rows with numbers shows whether the cell is judged to be a peak candidate (low shows that the cell is not a peak candidate and high shows that the cell is a apeak candidate.

Figure C.4 is also a screenshot of Vivado that shows an example of confirming whether the found peak candidates satisfy the required condition. The threshold of peak candidates was set to be 20, which means that the selected cell should have '1' more than or equivalent to 20 in the 25-bit array of peak candidates in this cell of the hough planes of all 25 layers. All the cells with '1' more than or equivalent to 20 were judged to be peak candidates in Figure C.4. Such comparisons are repeated to confirm that the found peak candidates satisfy the required conditions.

Appendix D

Optimization of the Parameters

Though Section 5.3 infers that the Full-hit 2D with default parameters can adapt to the operation at the targeted luminosity, the trigger rate reaches 7.0 kHz at BGx20, a beam background level one-third higher than the expected level at the targeted luminosity. Parameter tuning is conducted as an attempt to derive higher robustness to fake tracks with keeping the reconstruction efficiency.

Table D.1: The reconstruction efficiency and the fake track rate with BGx20 for each set of parameters. The trigger rate caused by fake tracks is simulated for the setting of parameters with reasonable efficiency and fake track rate. The size $a \times b$ means that the number of bins of φ_0 $(1/r)$ is a (b). The errors are statistical errors calculated by the Clopper-Pearson method.

N_{hits}	N_{cells}	Size(#bin)	efficiency	fake track rate	trigger rate
20	2	160×34	$0.994^{+0.002}_{-0.004}$	$0.204^{+0.014}_{-0.013}$	$6.0^{+3.6}_{-2.4}$
20	3	160×34	$0.991^{+0.003}_{-0.004}$	$0.187^{+0.013}_{-0.012}$	
20	5	160×34	$0.922^{+0.009}_{-0.009}$	$0.130^{+0.012}_{-0.011}$	
20	7	160×34	$0.476^{+0.016}_{-0.016}$	$0.092^{+0.010}_{-0.009}$	
19	2	160×34	$0.997^{+0.002}_{-0.003}$	$0.339^{+0.016}_{-0.015}$	
20	2	320×68	$0.991^{+0.003}_{-0.004}$	$0.051^{+0.008}_{-0.007}$	$2.0^{+2.6}_{-1.3}$
20	3	320×68	$0.990^{+0.003}_{-0.004}$	$0.045^{+0.008}_{-0.007}$	$2.0^{+2.6}_{-1.3}$
20	5	320×68	$0.840^{+0.012}_{-0.012}$	$0.008^{+0.004}_{-0.003}$	
20	7	320×68	$0.624^{+0.016}_{-0.016}$	$0.001^{+0.0023}_{-0.0008}$	
20	2	480×102	$0.446^{+0.016}_{-0.016}$	$0.000^{+0.002}_{-0.000}$	
20	1	480×102	$0.804^{+0.013}_{-0.013}$	$0.069^{+0.009}_{-0.008}$	
20	2	400×84	$0.936^{+0.002}_{-0.003}$	$0.0037^{+0.007}_{-0.006}$	$0.00^{+0.18}_{-0}$
19	2	400×84	$0.989^{+0.003}_{-0.004}$	$0.024^{+0.008}_{-0.007}$	$1.0^{+2.3}_{-0.8}$

As the motive is to prepare for the underestimation of the beam background level at the targeted luminosity, we only simulate the events with a beam background level of BGx20. The reconstruction efficiency and the fake track rate with BGx20 for some of the settings of parameters are shown in Table D.1. For some of the settings of parameters with reasonable performance, the trigger rate caused by fake tracks is simulated.

Both increasing of N_{cells} and the number of bins can suppress the fake track rate, but damage reconstruction efficiency at the same time. Compared with increasing of N_{cells}, increasing the number of bins show a more significant effect on reducing the fake track rate with a smaller drop of reconstruction efficiency.

The improvement of the Full-hit 2D comes from making use of the inner hit-patterns of track segment hits. However, it is meaningless if the adjacent CDC hits pass through the same cells in the hough grid, in which case the two adjacent

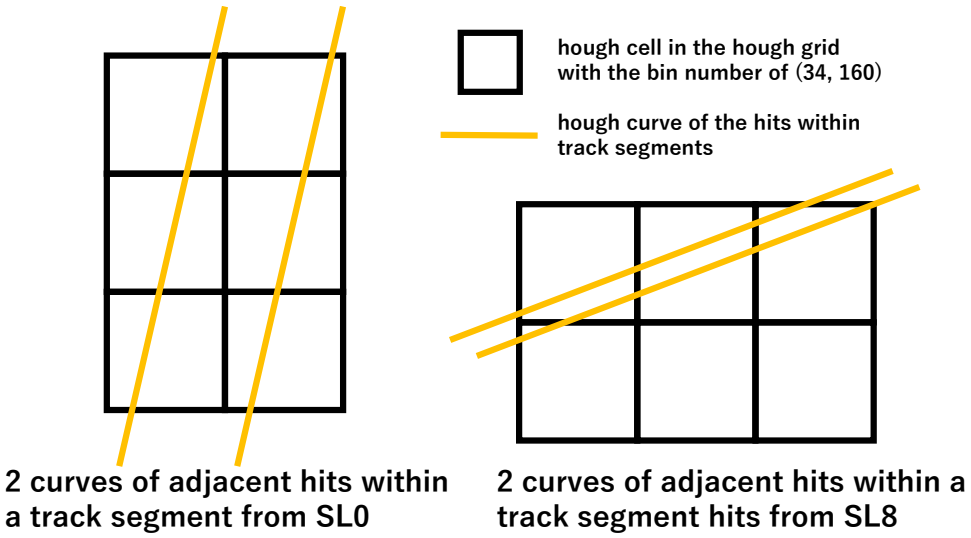

Figure D.1: The black squares are the hough cells in the hough grid with the number of bins of (34,160). The orange curves are hough curves determined by Eq. 3.2 in which the track segment hit is substituted by the CDC hit in a track segment hit. The left picture shows the two curves of adjacent CDC hits at the same layer within a track segment from SL0 and the right picture shows the two curves of adjacent CDC hits at the same layer within a track segment from SL8.

CDC hits can hardly be discriminated. As shown in Fig. D.1, with the default number of bins, the slope of the curve from SL8 is small and the distance between them in the φ_0 direction is smaller than half of the bin length. The two facts diminish the distinction between the adjacent CDC hits from outer layers.

The reconstruction efficiency drops significantly to 44.6% if the number of bins increases to 480×102. It is expected because too small hough cells prevent peak candidates from clustering together as interpreted in Section B.1. If the N_{cells} decreases to 1, the reconstruction efficiency increases back to 80.4% as expected according to the interpretation in Section B.1.

A proper set of the number of bins with better suppression of fake tracks than 320×68 while not having a significant drop of reconstruction efficiency like 480×102 has been found to be 400×84. N_{hits} of 20 and the number of bins of 400×84 can strongly suppress the fake track rate down to 0.37%. Fake tracks can hardly be reconstructed with such a low fake track rate. Triggered events are not found within 10,000 sample events, which totally corresponds to a time span of 0.01 ms. Though there is a small loss of reconstruction efficiency that decreases to 93.6%, decreasing N_{hits} to 19 can increase the reconstruction efficiency back to 98.9% with still more excellent fake track of 2.4% rate than other sets of parameters.

These settings of parameters serves as backup options if the beam background level at targeted luminosity is higher than expected.